MANIPULATION OF SOUND PROPERTIES BY ACOUSTIC METASURFACE AND METASTRUCTURE

JIAJUN ZHAO

(B.Eng., Nanjing University)

A THESIS SUBMITTED

FOR THE DEGREE OF DOCTOR OF PHILOSOPHY

DEPARTMENT OF ELECTRICAL AND COMPUTER ENGINEERING

NATIONAL UNIVERSITY OF SINGAPORE

2015

Declaration

I, JIAJUN ZHAO, hereby declare that this thesis is my original work and it has been written by me in its entirety. I have duly acknowledged all the sources of information which have been used in the thesis.

This thesis has also not been submitted for any degree in any university previously.

Signed: 

Date:

January 2016

Acknowledgements

It is my great pleasure to thank everyone who has kindly helped me during my PhD period. First and foremost, I would like to sincerely thank Dr. Cheng-Wei Qiu (National University of Singapore) and Dr. Baowen Li (University of Colorado Boulder). Dr. Qiu and Dr. Li are very supportive of my research and have given me the freedom to pursue various projects without objection. They have also provided insightful discussions on my research. I am also very grateful to Dr Zhi Ning Chen (National University of Singapore/Institute for Infocomm Research) for his scientific advice and knowledge, and many discussions and suggestions.

I specially would like to thank all my colleagues at NUS for their invaluable advice. A special thank you to Qasim Mehmood and Mohammad Danesh, for the great memories together and the sincere friendship. My thanks also go out to the support I am receiving from the University of Texas at Austin, where I am now working as a research scholar. I am especially grateful to Dr. Harry Swinney, Dr. Likun Zhang and Dr. Michael Allshouse for their patience, motivation, and immense knowledge in science. I am also deeply grateful to my parents for their constant encouragement and endless love.

I acknowledge the support of the Presidential Fellowship I am granted with by NUS and Singapore. For the non-scientific side of my thesis, I particularly want to thank "Living Stone" in Nanjing, "CPBC" in Singapore and "Gracepoint" in Austin for their encouragement. Special thanks to Tim Fitz, Debbie Fitz, Hongning Zhu, Dr. Franco Lim, George Butron, Susanna Lee and Dr. Jonathan Lee.

Summary

Manipulation of sound properties has attracted the interest of acoustical engineers for a long time. Using the mathematical method called transformation acoustics, researchers have demonstrated a host of striking unprecedented devices with unusual sound properties and phenomena, such as negative density, negative bulk modulus, extraordinary sound transmission, super resolution, etc. These devices that are engineered to have acoustic properties not yet found in nature are called acoustic metamaterials. Here, we extend the concept of metamaterial to metasurface and metastructure, which are made from assemblies of various elements fashioned from traditional materials such as copper or membrane.

Different from acoustic metamaterial which enables abnormal sound properties inside itself, the proposed acoustic metasurface is a thin-layer structure which allows the change of sound properties right at its surface. Thus, instead of gradual change inside metamaterial, acoustic waves seem to have an abrupt change after touching metasurface.

Besides, inasmuch as acoustic metamaterial is based on transformation acoustics, the conformal mapping of coordinates inevitably leads to complex parameters. Realizing these parameters in metamaterial is usually challenging. Here, we also propose the concept of acoustic metastructure, which does not rely on transformation acoustics. By a unique design, the

acoustic metastructure has a much accessible layout and does not have components of microscopic or smaller scales.

The work done related to the thesis during my doctoral program includes: theoretically and simulationally constructing the acoustic metasurface of inhomogeneous acoustic impedance for various applications such as acoustic disguise, acoustic planar lenses, acoustic ipsilateral imaging, and the conversion from propagating to surface acoustic waves; extending the prior proposed structure to be three dimensional, resulting in the out-of-incident-plane fluid-particle vibration; optimizing acoustic focusing for medical and industrial applications such as focused ultrasound surgery, lithotripsy, and nondestructive testing; proposing a density-near-zero metastructure to provide an accessible way for acoustic cloaking.

In this thesis, we elaborate the design of acoustic metasurface and metastructure, and their functionality in manipulation of sound properties. In Chapter 1, the background of the research is given; In Chapter 2, a metasurface with inhomogeneous acoustic impedance is proposed to achieve acoustic wavefront manipulation; In Chapter 3, a metasurface is designed to tweak the vibrational orientation of sound; In Chapter 4, an active metasurface piezoelectric transducer is used to control acoustic focusing; In Chapter 5, the near-zero density is obtained by a metastructure; In Chapter 6, we envision some possible future works.

Contents

List of Tables

List of Figures

List of Abbreviations

1D	one dimension; one-dimensional
2D	two dimension; two-dimensional
3D	three dimension; three-dimensional
SAI	specific acoustic impedance
GSL	generalized Snell's law of reflection
IGSL	impedance-governed generalized Snell's law of reflection
PAW	propagating acoustic wave
SAW	surface acoustic wave
FEM	finite element method
PT	piezoelectric transducer
RSI	acoustic Rayleigh-Sommerfeld diffraction integral
BPSO	binary particle swarm optimization
FWHM	full width at half maximum
PZT	lead zirconate titanate
B.C.	boundary condition
DNZ	density near zero
EST	extraordinary sound transmission

List of Symbols

ω	angular frequency	rad/s
p	acoustic pressure	Pa
p_{ro}	p of ordinary reflection	Pa
θ_{ro}	angle of ordinary reflection	rad
p_{re}	p of extraordinary reflection	Pa
θ_{re}	angle of extraordinary reflection	rad
p_i	p of incident sound	Pa
θ_i	angle of incident sound	rad
ρ_w	density of water	kg/m^3
ρ_a	density of air	kg/m^3
c_0	speed of sound	m/s
d	discretized spacing	m
Z_n	specific acoustic impedance	Pa·s/m
λ	wavelength	m
k_0	wave number	rad/m
f	frequency	Hz
V_0	amplitude of electric potential	J/C
γ	damping coefficient	1/s

Chapter 1

Introduction

Engineering the wavefronts of both electromagnetic and acoustic waves has long captivated the increasing interest and popularity, such as cloaking, illusion, focusing, etc. Among various schemes proposed to manipulate the light, the generalized Snells law has recently been reformulated [1]. This mechanism opens up new initiatives in realizing negative reflection and negative refraction, as well as other possibilities in optical wave engineering.

However, there are a few critical problems in this optical scheme: the abrupt phase change relies on the metallic subwavelength structures, which is not scalable into other wave forms; the interesting new result derived from this generalized Snells law is only associated to the anomalous reflected/refracted components, which is very low in intensity.

In principle, all those phenomena can be explained in terms of using a phased antenna array to steer its beam directions in classical electromagnetism. Hence, the only unexplored wonderland is in the acoustic domain, which cannot be simply included in the antenna engineering perspective.

This chapter addresses the background of my thesis work in acoustics. Sections 1.1 to 1.4 correspond to the introductions to Chapter 2 - 5, respectively. Section 1.5 addresses the outlines of Chapters 2 - 5.

1.1 Reshaping wavefronts in optics and acoustics

Refraction in classic optics was recently revisited from the viewpoints of complex refractive index of a bulky medium [2], abrupt phase change of an interface [1], and diffraction theory for gratings [3, 4]. Furthermore, these works shed light on the relation between the reflection and incidence, interpreted as the generalized Snell's law of reflection (GSL) [1], a novel way to optical wavefront engineering, resulting in promising accomplishments [5–9]. In optics, the phase-inhomogeneous metasurfaces realized by thin metallic nano-antennas conserve the wave number along an interface while impose the extra phase accumulation [1]. Fundamental physics is explained by a phased antenna array [10].

In principle, GSL is based on Fermat's principle, which holds for all monochromatic waves. However, the luxury of using metallic metasurfaces [1, 5] to fulfill the optical phase control is no more available in acoustics due to the limited choice of acoustic materials. Thus, the variable in GSL: the phase change on a flat surface becomes an abstract concept in acoustics without any design principle and practical clue. Therefore, it is indispensable and valuable to establish a different principle to manipulate acoustic waves.

1.2 Vibrational direction in fluids and solids

When an acoustic wave with a certain frequency is excited in fluids, the fluid particles will experience a restoring force, hence oscillating back and forth in a monochromatic way. The orientation of such longitudinal oscillation is the vibrational direction of a fluid particle. The vibration is undoubtedly an important characteristic of acoustic waves (like the polarization for electromagnetic waves). In electromagnetism, we can manipulate polarization by conventional methods such as dichroic crystals, optical gratings, or birefringence effects, etc [11, 12]. In elastic waves, we can also reach the mode conversion because the molecules in solids can support vibrations in various directions [13, 14]. However, when sounds propagate freely in fluids, few attempts were made so far toward tweaking the vibrational orientation, since the compression mode along the incident plane is considered to be the only possibility in acoustics. On the other hand, being enabled by the flexible dispersion of metamaterials, acoustic metamaterials can have solid-like transverse modes at density-near-zero [15] while conversely elastic metamaterials can have a fluid-like longitudinal mode when the elastic modulus goes negative [16] to allow polarization conversion. However, these metamaterials require resonating units, which have to be specially designed to balance possible loss.

Nevertheless, if one can tweak the reflected sound out of the incident plane, the vibrational direction, though still longitudinal with respect to the reflected beam itself, can therefore be manipulated accordingly. In other words, we can yield perpendicular vibration components in reflection with respect to the incident vibration, and control the spatial angle of such out-of-incident-plane vibration. In this connection, we propose a scheme by

designing an acoustic flat metasurface reflector to manipulate the vibrational orientations generated by sound in fluids. Metasurfaces have drawn much attention recently in electromagnetism, such as frequency selective polarizers [17], the wave-form conversion [18], wavefront-engineering flat lens [19], and polarization converter [20]. The concept of acoustic metasurfaces was not well investigated before, owing to the intrinsic nature of compression modes and limited choices of natural materials.

1.3 Acoustic focusing and piezoelectric transducer

Research on acoustic focusing has led to various applications such as nondestructive testing techniques that inspect materials for hidden flaws [21–23]. Usually piezoelectric transducers (PTs) are the most commonplace devices serving as the actuators of acoustic focusing. As the mechanism, when an electric field is applied across piezoelectric materials, the polarized molecules will align with the electric field, causing the materials to change dimensions [24, 25]. Apart from the industrial applications, acoustic focusing utilized in medical science contributes significantly to therapeutic techniques as well. Ultrasound waves excited by PTs are capable of transmitting energy inside a body for medical purposes such as diagnostic sonography [26]. Other examples include focused ultrasound surgery that generates localized heating to treat tumors [27, 28], and lithotripsy that breaks up kidney stones [29].

To avoid the bulky size of a curved PT, the flat annular Fresnel PT has been invented over decades, reducing the volume of piezoelectric portions

into a flat layer [30]. However as the trade-off, Fresnel PT intrinsically cannot concentrate the excited acoustic energy completely, as it is always accompanied with higher-order diffraction. In detail, a planar PT using a Fresnel equal-spaced array will inevitably generate the parasitic multiple divergent beams and higher-order convergent beams, making the focal spots less applicable. Actually, there has been to date no such acoustic design technique that allows us to achieve arbitrarily designed focal pattern along the axis. For example, one expected focal pattern for ultrasonic surgery is a specific segment of high acoustic energy along the axis (both its distance away from the PT and its focal depth can be designed), i.e., an acoustic far-field focal needle, which was never obtained by PTs. A finite-length focal-needle pattern is also quite promising for particle operation and acceleration, which was developed in optics [31, 32].

Additionally, the focal resolution created with traditional PTs is usually low, whose focal size is much larger than one wavelength λ. Since the focal resolution can be improved with the wave frequency increased, previous researches usually ignore the consideration of improving the resultant focal resolution. However, it is noteworthy that an excitation of a higher frequency demands more energy consumption and suffers from stronger attenuation. Besides, acoustic aberration could also severely blur the focal resolution. Thus, the rational improvement is to increase the relative focal resolution with the same excited frequency remaining.

1.4 Invisibility cloaking in optics and acoustics

Various metamaterial-based invisibility cloaking has been demonstrated in optics, acoustics [33, 34] and heat conduction by the theory of transforming coordinates. As a trade-off, in optics, the spatially-tailored properties of metamaterials, usually inhomogeneous and anisotropic, impose challenging complexities in structural configuration and cloaking realization [33, 35]. As the acoustic analog of transformation optics [36], the experimental realization of acoustic cloaking was reported [37, 38], but its inhomogeneous acoustic inertia and modulus caused by coordinate transformation inevitably result in the same challenges as in optics. More recently, a topological-optimization method was invented to cancel acoustic scattering by wave interference [39, 40], which only requires a specific optimized distribution of rigid boundaries around the object to be hidden. Although this scheme does not require considering a complex structure of artificial metamaterials, topological acoustic cloaking highly relies on the shape and the locus of the object to be hidden. Therefore, the object actually is a part of the cloaking device itself. It implies that the cloaking structure designed for one object has to be redesigned for another which has different shapes, locus, or material composition.

To construct an isotropic acoustic cloak, independent of the cloaked objects in two-dimensional space or in curved waveguides, could be meaningful in both theory and application. For example, the isotropic acoustic cloak in free space could inspire the way of designing stealth planes or submarines for military purpose.

1.5 Outlines of Chapters 2 - 5

In Chapter 2, we unveil the connection between the acoustic impedance along a flat surface and the reflected acoustic wavefront, in order to empower a wide variety of novel applications in acoustic community. Our designed flat metasurface can generate double reflections: the ordinary reflection and the extraordinary one whose wavefront is manipulated by the proposed impedance-governed generalized Snell's law of reflection. The proposed law of reflection is based on Green's function and integral equation, instead of Fermat's principle for optical wavefront manipulation. Remarkably, via the adjustment of the designed specific acoustic impedance, extraordinary reflection can be steered for unprecedented acoustic wavefront while that ordinary reflection can be surprisingly switched on or off. The realization of the complex discontinuity of the impedance surface has been proposed using Helmholtz resonators.

In Chapter 3, we demonstrate a flat acoustic metasurface that generates an extraordinary reflection, and such metasurface can steer the vibration of the reflection out of the incident plane. When acoustic waves are impinged on an impedance surface in fluids, it is challenging to alter the vibration of fluid particles since the vibrational direction of reflected waves shares the same plane of the incidence and the normal direction of the surface. Our proposed flat acoustic metasurface can steer the vibration of the reflection out of the incident plane. Remarkably, the arbitrary direction of the extraordinary reflection can be predicted by a Greens-function formulation, and our approach can completely convert the incident waves into the extraordinary reflection without parasitic ordinary reflection.

In Chapter 4, we demonstrate the manipulation of focal patterns in acoustic far fields. It has a pivotal role in medical science and in industry to concentrate the acoustic energy created with piezoelectric transducers into a specific area. However, previous researches seldom consider the focal resolution, whose focal size is much larger than one wavelength. Furthermore, there is to date no such design method of piezoelectric transducer that allows a large degree of freedom to achieve designed focal patterns. Here, an active and configurable planar metasurface PT prototype is proposed to manipulate the acoustic focal pattern and the focal resolution freely. By suitably optimized ring configurations of the active metasurface PT, we demonstrate the manipulation of focal patterns in acoustic far fields, such as the designed focal needle and multiple focuses. Our method is also able to manipulate and improve the cross-sectional focal resolution from subwavelength to the extreme case: the deep sub-diffraction-limit resolution. Via the acoustic Rayleigh-Sommerfeld diffraction integral cum the binary particle swarm optimization, the free manipulation of focusing properties is achieved in acoustics for the first time. Our approach may offer more initiatives where the strict control of acoustic high-energy areas is demanding.

In Chapter 5, isotropic acoustic cloaking is proposed using a density-near-zero metastructure for extraordinary sound transmission. The metastructure for acoustic cloaking is made by single-piece homogeneous elastic copper, which can be detached and assembled arbitrarily. We theoretically and numerically demonstrate the cloaking performance by deploying density-near-zero metastructures in various ways in two-dimensional space as well as in acoustic waveguides. The density-near-zero material can make any inside objects imperceptible along sound paths. Individually and collectively,

the metastructure maintains both the planar wavefront and the nearly perfect one-dimensional transmission, in presence of any inserted object. The overall cloaked space can be designed by adding metastructures without the limit of the total cloaked volume.

1.6 My published journal articles related to thesis

1. J. Zhao, Z. N. Chen, B. Li & C. W. Qiu, *Journal of Applied Physics* (2015), DOI: 10.1063/1.4922120

2. J. Zhao, H. Ye, K. Huang, Z. Chen, B. Li & C. W. Qiu, *Scientific Reports* (2014), DOI: 10.1038/srep06257

3. J. Zhao, B. Li, Z. Chen & C. W. Qiu, *Scientific Reports* (2013), DOI: 10.1038/srep02537

4. T. Han, J. Zhao, T. Yuan, D. Y. Lei, B. Li & C. W. Qiu, *Energy and Environmental Science* (2013), DOI: 10.1039/c3ee41512k

5. J. Zhao, B. Li, Z. N. Chen & C. W. Qiu, *Applied Physics Letters* (2013), DOI: 10.1063/1.4824758

Chapter 2

Manipulating acoustic wavefront with metasurface of inhomogeneous impedance

This chapter establishes the framework of acoustic wavefront manipulation by resorting to the acoustic metasurface which has specific acoustic impedance (SAI) inhomogeneity and discontinuity, rather than the phase inhomogeneity in terms of wave propagation [1, 2]. SAI is one of the acoustic properties of materials, which is comparably more possible to be controllable in reality than propagation phase. More specifically, we find out that the inhomogeneous SAI will generally give rise to one ordinary reflection p_{ro} and one extraordinary reflection p_{re}, i.e., *double reflections*. Furthermore, the flat inhomogeneous SAI surface is able to switch on or off p_{ro} without the influence on its direction, but to tweak p_{re} in the manner of our proposed design principle: impedance-governed generalized Snell's law of reflection (IGSL) in acoustics.

2.1 Extraordinary reflection and ordinary reflection

The inhomogeneous SAI Z_n of the flat surface can be expressed as a complex, whose real and imaginary parts may change spatially. In order to reduce the complexity of modeling as the beginning attempt, we set the real part as a spatial constant. Later we prove that the spatial varying of the real part cannot support our results, which is derived in detail in Appendix A. We consider

$$Z_n(y,\omega) = A\left[1 - i\tan\frac{\psi(y)}{2}\right], \tag{2.1}$$

where A is an arbitrary constant irrelevant to any spatial change and $\psi(y)$ is the variable for the imaginary part.

Note that ω-dependency on the right hand side of Equation (2.1) has already been included in $\psi(y)$. The total acoustic pressure p in the upper space satisfies the integral equation:

$$\begin{aligned} p(y,z,\omega) \approx p_i + p_{ro} - \sqrt{\frac{k_0}{2\pi\sqrt{y^2+z^2}}}e^{i(k_0\sqrt{y^2+z^2}-\frac{\pi}{4})} \\ \times \frac{\rho_w c_0\cos\theta^*}{2A\cos\theta^* + \rho_w c_0} \times \int_{-\infty}^{\infty} e^{i\psi(y_0)}p(y_0,0,\omega)e^{-ik_0 y_0\sin\theta_{re}}dy_0, \end{aligned} \tag{2.2}$$

where p_i denotes the incidence; ρ_w and c_0 are the density and the speed of sound in the upper space in Figure 2.1(a); $k_0 = \omega/c_0$ is the wave number; θ^* is constant; θ_{re} is the angle of p_{re}. Both p_{ro} and p_{re} exist for a general

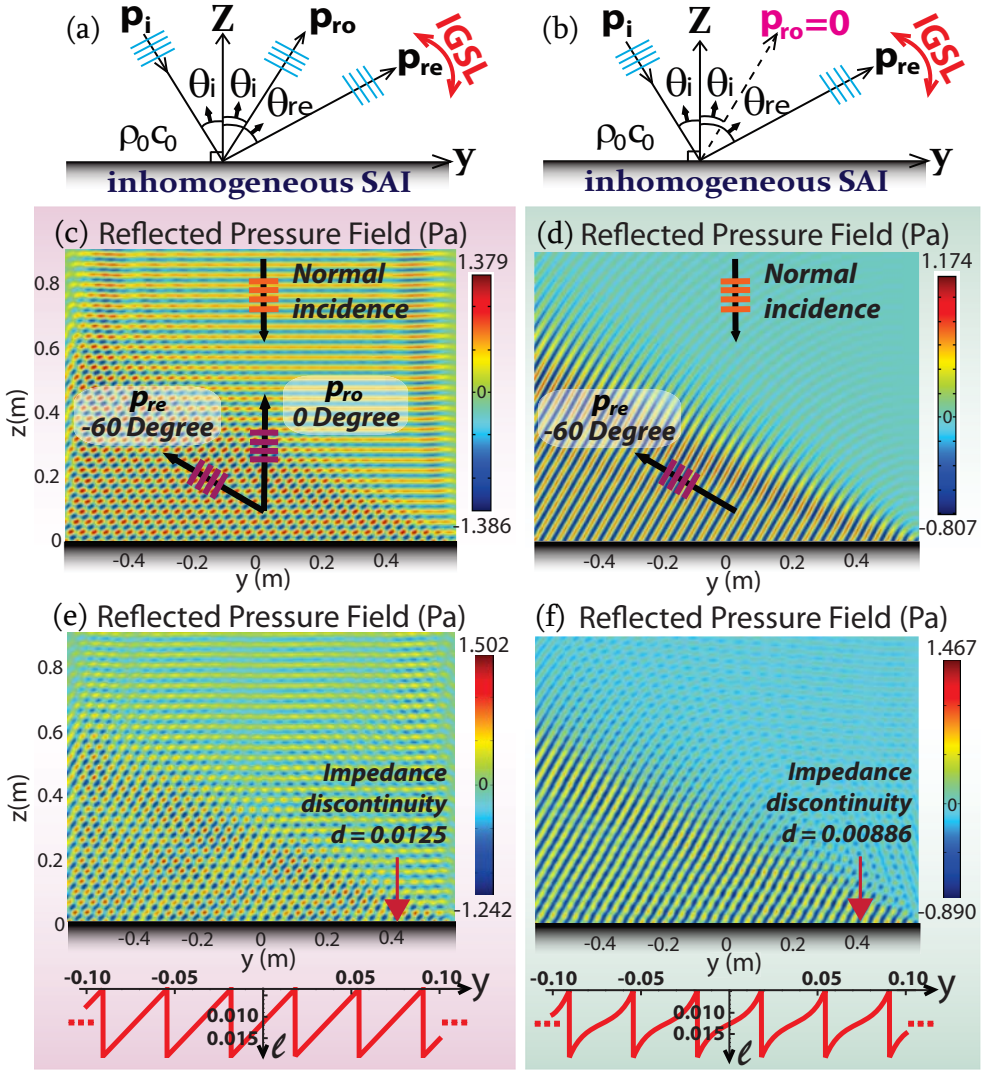

FIGURE 2.1: (a) For a flat interface with an inhomogeneous SAI, the angle of p_{ro}, i.e., θ_{ro}, is not influenced, while p_{re} occurs simultaneously and θ_{re} is controlled by IGSL. (b) If SAI is properly controlled, p_{ro} is null. (c) Ultrasound with unit amplitude and $\omega = 300Krad/s$ impinges upon SAI surfaces in water. The SAI along the flat surface generates both p_{ro} and p_{re} when an arbitrary A is chosen in Equation (2.1). (d) A particular SAI is chosen according to Equation (2.7). $\psi(y) = -100\sqrt{3}y$ is selected throughout. (e,f) Simulation results based on impedance discontinuity with relations between l and y enclosed, corresponding to the cases (c) and (d) respectively. Figure adopted and reproduced with permission from ref. [41].

A, implying the unusual *double reflections*:

$$p_{ro} \propto \frac{2A\cos\theta_i - \rho_w c_0}{2A\cos\theta_i + \rho_w c_0} \exp[ik_0(y\sin\theta_i + z\cos\theta_i)]; \tag{2.3}$$

$$p_{re} \propto \int_{-\infty}^{\infty} e^{i\psi(y)} e^{ik_0 y(\sin\theta_i - \sin\theta_{re})} dy. \tag{2.4}$$

Double reflection consists of one ordinary reflection p_{ro} and one extraordinary reflection p_{re}. Intuitively, the direct-current component of the surface impedance contributes to p_{ro} while the alternating-current component contributes to p_{ro}. After applying the first-order approximation and the stationary phase approximation to Equation (2.4), the relation between θ_{re} and the incident angle θ_i is unveiled:

$$\begin{cases} k_0(\sin\theta_{re} - \sin\theta_i) = d\psi(y)/dy \\ Z_n(y,\omega) = A\{1 - i\tan[\psi(y)/2]\} \end{cases}. \tag{2.5}$$

Note that the extraordinary reflection can exist only when the inhomogeneous SAI along the flat surface is expressed in form of Equation (2.1), on the basis of our derivation. Although IGSL's appearance is similar to GSL [1, 2, 5], its physical meaning of $\psi(y)$ is dramatically different. Fundamentally, the variable of our IGSL Equation (2.5) is about the value of surface acoustic impedance instead of the abrupt propagating phase change. Moreover, IGSL only serves to steer p_{re} at will, with no influence on the direction of p_{ro}, as illustrated in Figure 2.1(a). In Appendix B we highlight the irrelevance between GSL and our proposed IGSL. In addition, GSL mentions the extra accumulated phases along wave-propagation paths, but it is still relying on graphical methods to find out the relation between the

configuration of the passive antenna array and the needed phase in optics [1]. However, we do not have the passive antenna in acoustics. Here, IGSL Equation (2.5) and Equation (2.1), serving as an explicit design rule, provide us the feasible way based on a different mechanism in acoustics.

Equation (2.5) also sheds the light on an extreme angle (similar to critical angle):

$$\theta_e = \begin{cases} \arcsin(-1 - \frac{1}{k_0}\frac{d\psi(y)}{dy}), \text{if} \frac{d\psi(y)}{dy} < 0 \\ \arcsin(+1 - \frac{1}{k_0}\frac{d\psi(y)}{dy}), \text{if} \frac{d\psi(y)}{dy} > 0 \end{cases}, \tag{2.6}$$

above which p_{re} becomes evanescent in the upper space. Equation (2.6) holds only when $-1 \leq 1 - \frac{1}{k_0}\left|\frac{d\psi(y)}{dy}\right| \leq 1$. Otherwise, p_{re} becomes evanescent.

Usually, both p_{ro} and p_{re} will coexist as shown in Figure 2.1(a), suggesting *double reflections*, while IGSL only controls θ_{re}. Hence, it is interesting to eliminate p_{ro} as shown in Figure 2.1(b), by means of a particularly selected value of A. Equation (2.3) suggests that $A = (\rho_0 c_0)/(2\cos\theta_i)$ can make p_{ro} vanish, i.e., p_{ro} is switched off, as shown in Figure 2.1(b). The corresponding SAI of the flat surface then becomes

$$Z_n(y,\omega) = \frac{\rho_w c_0}{2\cos\theta_i}\left[1 - i\tan\frac{\psi(y)}{2}\right]. \tag{2.7}$$

2.2 Continuous and discontinuous impedance

Supposing the gradient of $\psi(y)$ along the flat interface is constant, we notice that Equation (2.4) turns out to be a Dirac Delta without any approximation. From Equation (2.5) we predict that the wavefront of p_{re} will propagate in the form of a plane acoustic wave, independent of y. We select

water ($\rho_w = 1000kg/m^3$; $c_0 = 1500m/s$ [42]) as the background medium, $\omega = 300Krad/s$ as the circular frequency, $e^{-ik_0 z}$ as the normal incident plane ultrasound, and a linear form $\psi(y) = -100\sqrt{3}y$ in Equation (2.7).

θ_{re} is theoretically found to be $-60°$ by IGSL, validated by our simulation in Figure 2.1(d). p_{ro} is thoroughly suppressed thanks to the specific A chosen according to Equation (2.1). In contrast, in Figure 2.1(c), the same parameters are kept except for another A, whose value is arbitrarily taken to be $\rho_w c_0$. It clearly shows that p_{ro} occurs and interferes with p_{re}, but p_{re} still keeps the same, verifying our theoretical formulation. In terms of phenomena, the designed inhomogeneous SAI Equation (2.1) essentially implies the changes of both the propagating phases and amplitudes, only by which the effect of double reflections may occur. In terms of physics, the extra momentum supplied by the metasurface is employed to compensate the momentum mismatch between the incident acoustic beams and the diffracted beams. Therefore, for the double backward propagating beams, p_{ro} is the commonplace reflection, while p_{re} is attributed to the diffraction of higher order.

Figure 2.1(d) suggests the possibility of negative reflection for p_{re}, which is further verified for oblique incidence in Figure 2.2. In Figure 2.2(a), because of the inhomogeneous SAI and the arbitrary A in Equation (2.1), both p_{ro} and p_{re} occur. Figure 2.2(b) depicts the same situation except for p_{ro} being switched off as a result of the specifically chosen A according to Equation (2.7), while the red line p_{re} stays the same as that in Figure 2.2(a). The blue braces represent the region of negative p_{re}. It is noteworthy that p_{re} does not exist if θ_i is beyond the extreme angle $\theta_e = -30°$ in Equation (2.6), corresponding to the purple dots.

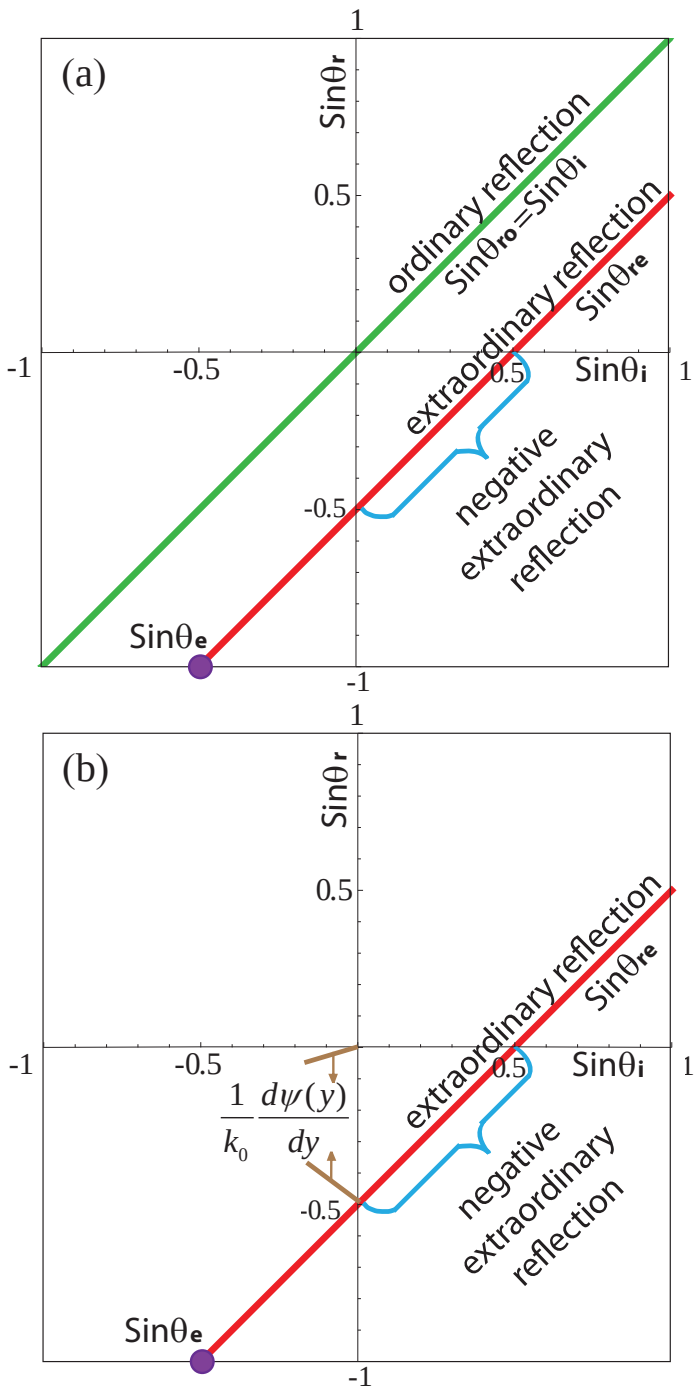

FIGURE 2.2: $\sin\theta_{ro,re}$ versus $\sin\theta_i$ when $k_0 = 10rad/m$ and $\psi(y) = -5y$. p_{ro} and p_{re} emerge simultaneously in (a). In (b), only p_{re} occurs for the same parameters of (a) except A. The purple dot denotes $\sin\theta_e$ in Equation (2.6). Figure adopted and reproduced with permission from ref. [41].

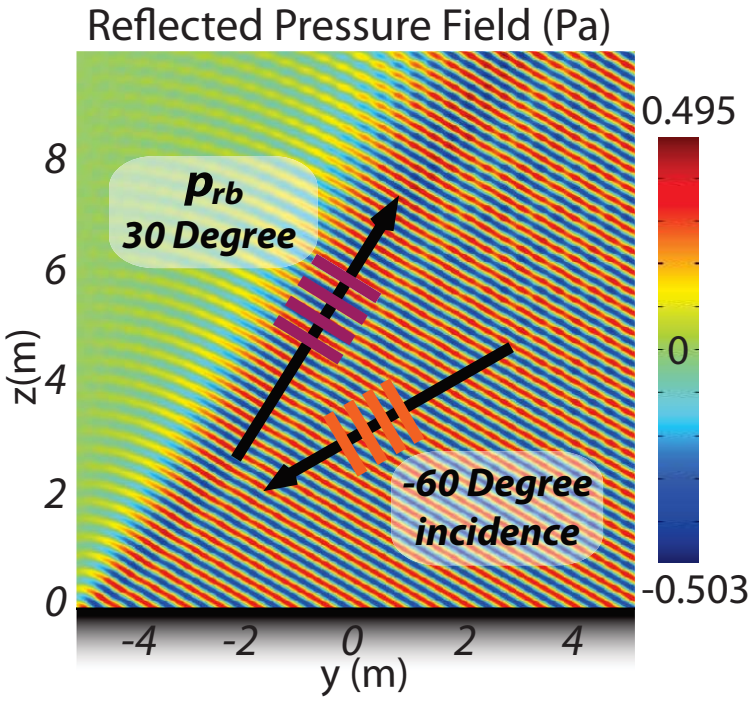

FIGURE 2.3: The SAI Equation (2.1) with $\psi(y) = (10 + 10\sqrt{3})y$ is set along the flat surface $z = 0$. In the upper space, the medium is water ($\rho_w = 1000kg/m^3$; $c_0 = 1500m/s$). An audible plane wave with unit amplitude and $\omega = 30Krad/s$ is $-60°$ obliquely incident. Only reflected acoustic pressure is plotted. The propagating path of p_{re} is noted as an arrow with purple crossbars. Figure adopted and reproduced with permission from ref. [41].

The field simulation for oblique incidence is shown in Figure 2.3. For this simulation we assume water ($\rho_w = 1kg/m^3$; $c_0 = 1500m/s$ [42]) as the background medium in the upper space. The SAI with the linear parameter $\psi(y) = (10 + 10\sqrt{3})y$ is set along the flat metasurface, and an audible ($\omega = 30Krad/s$) plane wave with a unit amplitude is obliquely incident with the incident angle $-60°$. These parameters theoretically lead to the angle of p_{re} 30° according to our proposed IGSL. Furthermore, p_{ro} vanishes thanks to the specific A chosen in Equation. (2.1). In Figure 2.3, we find out the simulation confirms the prediction via IGSL accurately, and p_{ro} disappears as expected.

Moreover, the incident audible plane wave and p_{re} are at the same side of the normal line, confirming the possibility of the negative extraordinary reflection. The singularity due to $\tan[\psi(y)/2]$ in the imaginary part of Equation (2.1) does not play a significant role because the mathematical singularity $\pm i\infty$ just occurs at singular positions, physically meaning the total reflection (reflection coefficient equals +1).

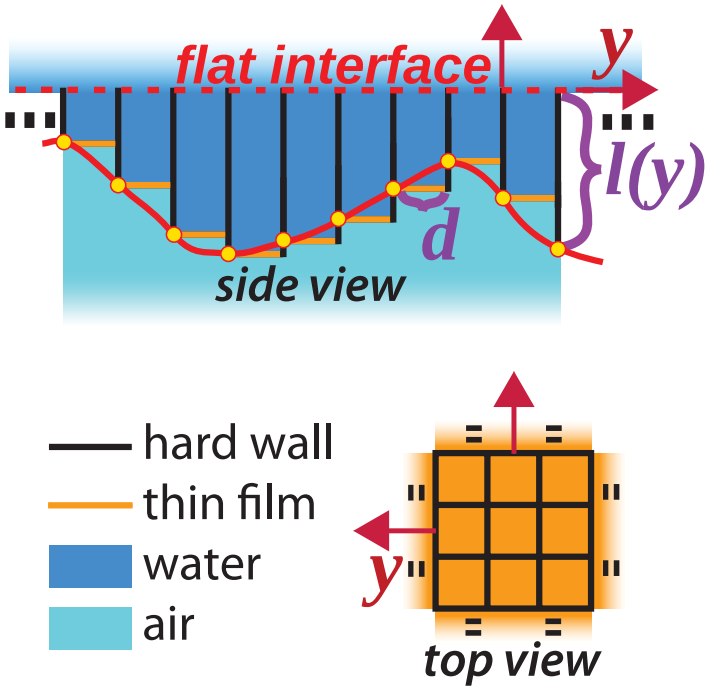

FIGURE 2.4: Realization schematics by hard-sidewall tubes of designed lengths. Figure adopted and reproduced with permission from ref. [41].

As depicted in Figure 2.4, we propose one plausible realization schematic for the general SAI of Equation (2.1), where all hard-sidewall tubes with one pressure-release termination are gathered and juxtaposed perpendicular to the flat interface. Observed at the top view, each tube has a square cross section whose width is d, with four enclosed hard sidewalls (black). Then observed at the side view, the upside open termination of each tube constitutes an effective SAI pixel of the interface, while the other end sealed by a thin film (orange) serves as the pressure-release termination. [42] The upper space and the interior of each tube are filled with water, without separation. The light blue indicates air downside, which is isolated from water by the thin film.

The SAI of each tube at the opening facing the upper space is [42]:

$$Z_t(y,\omega) = \frac{\rho_w c_0 {k_0}^2 d^2}{2\pi} - i\rho_w c_0 \tan\left[k_0 l(y) + k_0 \Delta l\right], \tag{2.8}$$

where $l(y)$ is the length of each tube and $\Delta l \approx 0.6133 d/\sqrt{\pi}$ is the effective end correction. By comparison of Equation (2.1) and Equation (2.8), it is required that $A = \rho_w c_0 {k_0}^2 d^2/(2\pi)$ and $A\tan[\psi(y)/2] = \rho_w c_0 \tan\left[k_0 l(y) + k_0 \Delta l\right]$, leading to the value of the spacing d for impedance discretized spacing and the dependence between $l(y)$ and $\psi(y)$:

$$\begin{cases} d = \sqrt{(2\pi A)/(\rho_w c_0 {k_0}^2)} \\ l(y) = \frac{1}{k_0}\arctan[\frac{{k_0}^2 d^2}{2\pi}\tan\frac{\psi(y)}{2}] + \frac{n\pi}{k_0} - \Delta l \end{cases}, \tag{2.9}$$

where the arbitrary integer n is required to be set suitably to make l a positive value. Thus, the change of ψ along y, representing the control of p_{re}, is interpreted as the change of l, implying one straightforward realization based on discontinuous impedance. Thus, the inhomogeneity of the

acoustic impedance is strictly paraphrased into the inhomogeneity of the tube-array structure, resulting in our acoustic metasurface. At the side view in Figure 2.4, the solid red contour indicates one arbitrary function of $l(y)$ calculated from Equation (2.9). Based on the discretized spacing d calculated from Equation (2.9) as well, we are able to find d and the corresponding height $l(y)$, marked with the yellow dots. The width of tubes, d, is required to be in subwavelength, which means that the criterion $A < 2\pi\rho_w c_0$ needs to be satisfied. The parameters d used in our simulations satisfy this criterion after compared with wavelengths. Also, note that the top of the tube array is aligned into a flat surface (red dashed line), above which acoustic waves impinge. Thus, the change of tube lengths will not affect the flatness of the surface. In addition, thanks to the property of the arc-tangent in Equation (2.9), the tube-array metasurface is within a thin layer without the space-coiling-up technique [43].

It is also noteworthy that because of the intrinsic differences between optics and acoustics, so far we cannot obtain the mechanism-analog of the optical metasurface, which is based on resonances and independent with the thickness or effective propagating lengths, but we can achieve the phenomenon-analog in acoustics using the tube array. In principle, because tubes can be regarded as Helmholtz resonators, complex SAI at each pixel can be realized by a suitable arrangement of resonators, as the analog of the complex electric impedance realized by the combination of resistance, capacitance and inductance. In addition, we know that only the real part, the electric resistance, consumes energy while the imaginary part does not. In the same manner in acoustics, the energy loss is theoretically only attributed to the real part of the surface complex SAI in Equation (2.8), i.e., the loss in our case is caused by the energy consumption from the tube array.

Using this method, we reproduce Figure 2.1(c,d) by realistic impedance discontinuity, so as to verify our proposed realization. In Figure 2.1(e,f), $d = 0.0125$ and 0.00886 are selected respectively according to Equation (2.9), and the corresponding contours of the tube length l in terms of the location y are illustrated as the red lines, respectively. Figure 2.1(e) shows strong interference between p_{re} and p_{ro} while Figure 2.1(f) shows the nearly undisturbed p_{re}, coinciding with Figure 2.1(c,d), respectively.

2.3 Acoustic illusion and ipsilateral focusing

To demonstrate IGSL's capability of designing novel acoustic devices, we metamorphose acoustic pressure fields everywhere through SAI manipulation as simulated in Figure 2.5. This deceptive effect is obtained by manipulating plane wavefronts into the wavefronts generated by a virtual reflector or focusing illumination, governed by the control of p_{re}, i.e., IGSL. Under these scenarios, we need to consider nonlinear forms of $\psi(y)$. New phenomena are thus expected when θ_{re} becomes spatially varying.

It is found that the acoustic deception can be created via IGSL, e.g., $\psi(y) = 0.7y^2$ in Equation (2.7), resulting in $p_{ro} = 0$. Correspondingly, θ_{re} in Figure 2.5(a) is a position-dependent function $\sin\theta_{re} = 0.14y$, in which case p_{re} fans out as demonstrated in Figure 2.5(a), verifying our theory. Here the discretized spacing d for impedance is 0.1772 and the relations between l and y derived from Equation (2.9) are enclosed in Figure 2.5. Therefore, IGSL can be employed to camouflage a flat surface as if there were a curved lens at the origin instead of the physical planar interface.

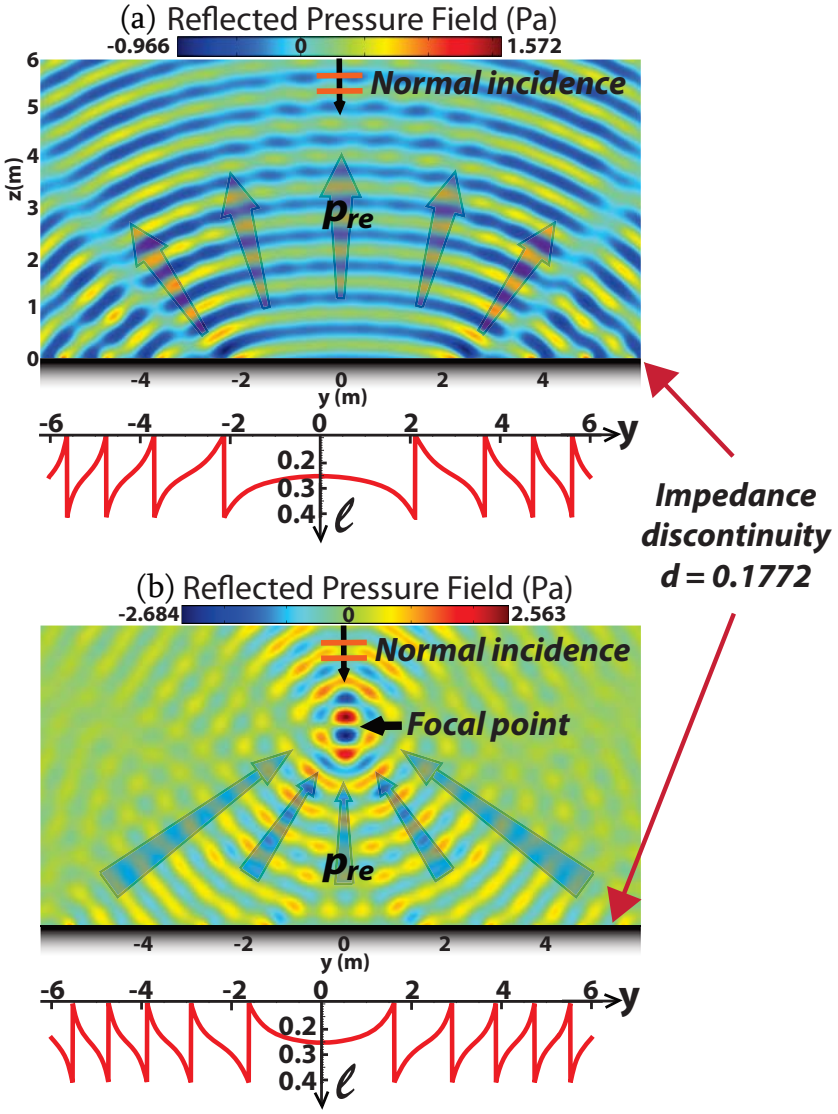

FIGURE 2.5: Wavefront metamorphosis via SAI interface, with impedance discontinuity $d = 0.1772$. A plane acoustic wave of $\omega = 15Krad/s$ is normally incident in water. Only reflected acoustic pressure is plotted. (a) The SAI of Equation (2.7) with $\psi(y) = 0.7y^2$ is set along the flat surface. p_{re} diverges into a curved wavefront. (b) The SAI of Equation (2.7) with $\psi(y) = -10\left(\sqrt{y^2+4^2}-4\right)$ is set. p_{re} converges to a focal point in the 2D case. Figure adopted and reproduced with permission from ref. [41].

The dual effect allowing a curved reflector to mimic a flat mirror, by manipulating the convex wavefronts into planar wavefronts, was reported in plasmonic regime [44].

Furthermore, the SAI can be designed to make acoustic waves reflected by a planar interface focused as well. In optics, a flat lens with metallic nanoantennas of varying sizes and shapes can consequently converge the transmitted light to a focal point [6, 7]. Note that the optical focusing controlled by optical GSL is on the other side of incoming lights, i.e., on two sides of the flat surface [6, 7] in the transmission mode. In acoustics, we employ an inhomogeneous SAI flat surface to focus p_{re}, in the reflection mode by IGSL without p_{ro}.

This *ipsilateral focusing* in Figure 2.5(b), is thus obtained in the planar geometry in acoustics for the first time. In Equation (2.7), a hyperbolic form is set: $\psi(y) = -k_0\left(\sqrt{y^2+f^2}-f\right)$ (f being the given focal length for the SAI of the flat interface. p_{re} from different angles constructively interferes at the ipsilateral focal point, as if the waves emerge from a parabolic surface. The parameters in Figure 2.5(b) are the same as those in Figure 2.5(a) except for the specific hyperbolic SAI form $\psi(y) = -10\left(\sqrt{y^2+4^2}-4\right)$, with the designed focal point at $(y = 0, z = 4)$ and p_{ro} suppressed. In addition, the simulated acoustic pressure by discretized impedance at the focal point is well confined at $(y = 0, z = 4)$.

Interestingly, the imaging at the same side was previously presented for electromagnetic waves [45, 46]. In [45], it demands strong chiral materials filled in the whole upper space. The same-side imaging is only a partial imaging, i.e., only one circularly polarized wave being imaged and the other being reflected ordinarily. In acoustics, our ipsilateral imaging is achieved

by translating all the stringent requirements of the half-space chiral materials into an inhomogeneous impedance surface. In electromagnetism, ipsilateral imaging can be achieved as well by surface gratings [46] or antenna arrays. However, the polarization of incident electromagnetic waves is always closely related to the effect of focusing. Therefore, the ipsilateral imaging in acoustics by IGSL has no polarization constraints thanks to the acoustic wave nature, i.e., longitudinal vibration.

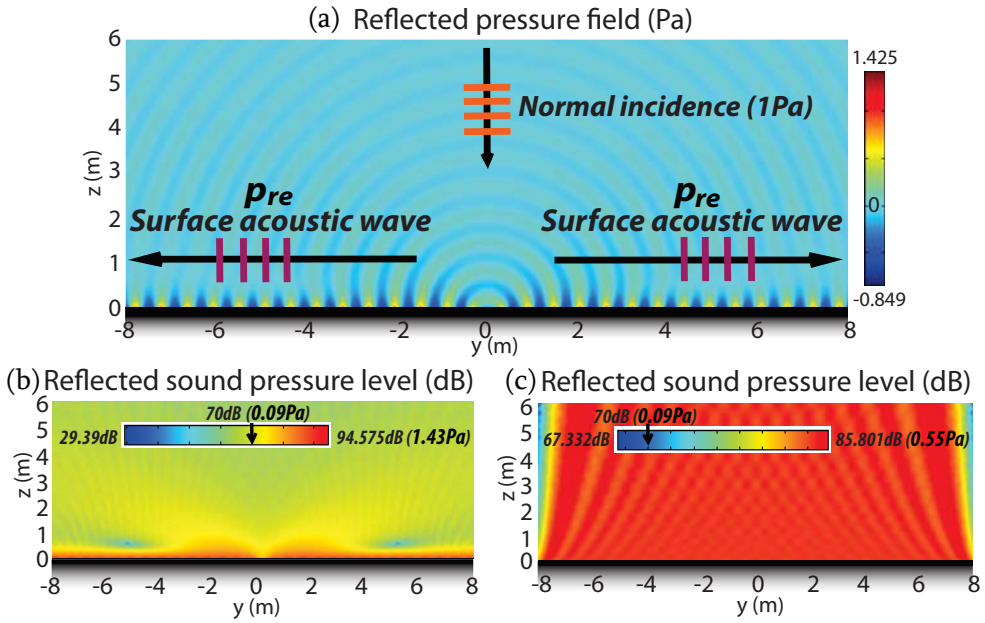

FIGURE 2.6: Conversion from PAWs to SAWs via SAI interface. The PAW with unit amplitude and $\omega = 15Krad/s$ is normally incident in water. Only reflected acoustic pressure is plotted. (a) The SAI of Equation (2.7) is set to be $\psi(y) = -11y$ for $y < 0$ and $\psi(y) = 11y$ for $y > 0$. SAWs are bifurcated at the origin and confined near the surface. (b) The reflected sound pressure level of (a). (c) The reflected sound pressure level when a homogeneous SAI is adopted instead. Figure adopted and reproduced with permission from ref. [41].

2.4 Conversion from propagating to surface waves

Beyond the acoustic-field metamorphosis, we further establish a kind of acoustic cognitive deception about an SAI surface converting propagating acoustic waves (PAW) to surface acoustic waves (SAW) in Figure 2.6, by means of IGSL. The extreme angle 0° in Equation (2.6) demands $\psi(y) = \pm 10y$. Therefore, we set the SAI of Equation (2.7) slightly over that extreme, e.g., $\psi(y) = -11y$ for $y < 0$ and $\psi(y) = 11y$ for $y > 0$ are set along the flat interface symmetrically with respect to the z. In Figure 2.6(a), the bidirectional surface acoustic waves are attributed to the coupling effect governed by the diffracted evanescent p_{re} which propagates along the metasurface [47]. Owing to the inhomogeneous SAI interface, the ideally perfect conversion comes true in acoustics except for a little diffraction. Physically, the SAI along the flat surface provides an extra momentum to compensate the momentum mismatch between propagating waves and surface waves in acoustics, resulting in the high efficiency conversion. In contrast, if one uses a constant SAI Equation (2.7) with $\psi(y) = 11$ along the flat surface (the homogeneous SAI does not generate p_{re}; only p_{ro} occurs), the reflected sound pressure level in Figure 2.6(c) is almost uniformly spread over the space.

Figure 2.6(b) clearly demonstrates that the acoustic field is well confined in the region close to the interface and attenuated quickly to around $0Pa$ away from the interface, revealing the nearly perfect conversion. Interestingly, it shows in [18] that the electromagnetic-varying metasurface is able to prevent the propagating electromagnetic waves from being reflected back to

the upper space. Hence, our PAW-SAW conversion in acoustics, originating from a distinguished mechanism, is differentiated from [18].

In Figure 2.6, we notice that such technology is functional as an alternative invisible acoustic cloak by trapping the acoustic field in the vicinity of the coating, resulting in much lower signal levels of reflection. It may pave the avenue to the large size acoustic invisibility since it is only dependent on the surface technique instead of wave-interaction based metamaterial acoustic cloaking [37]. It will also be promising to consider the time-varying surface technique in acoustics with nonreciprocal diffraction [48] in the future.

2.5 Methods

For theoretical derivations, we used Green's function, the integral equation Equation (2.2) and Born approximation. The detailed theoretical development is elaborated in Appendix A. For the numerical calculations, we used the Finite Element Method by means of the commercial software COMSOL Multiphysics. The left, right and top sides of the meshed domain are set as plane wave radiation conditions, while the bottom side is set as the impedance boundary with a certain value.

2.6 Conclusion and discussion

We have proposed the acoustic metasurface of inhomogeneous acoustic impedance. Impedance-governed generalized Snell's law of reflection has been established for manipulation of acoustic wavefronts. Due to the lack of

abrupt-phase-changing surface structures in acoustics, we resort to acoustic impedance as the variable to tweak sound reflection. Impedance-governed generalized Snell's law of reflection, which can simultaneously generate the switchable p_{ro} and the steerable p_{re}, provides us the explicit connection between our designed specific acoustic impedance and the reflected field, serving as the design rule in acoustics. We not only demonstrate intriguing acoustic manipulations but also provide insightful realization schemes of the metasurface. As a few examples, we demonstrate acoustic disguise, acoustic planar lens, acoustic ipsilateral imaging, and the conversion from propagating to surface acoustic waves.

Ultra-thin acoustic metasurfaces can also be constructed by the method of coiling up space, so that sound trajectories can be altered by changing wave propagating paths [49, 50]. This method provides a more accessible way to steer acoustic wavefronts than our proposed approach, but the trade-off is the lack of capability to generate rich phenomena such as double reflections demonstrated in this thesis.

Chapter 3

Redirecting acoustic waves out of the incident plane

This chapter addresses a flat metasurface to manipulate the extraordinary out-of-incident-plane reflection and vibration in acoustics, validated by the theoretical modeling and the numerical experiment. We theoretically demonstrate that in fluids, extraordinarily reflected sound waves can be achieved along a three-dimensional spatial angle out of the incident plane by manipulating the impedance distribution of a flat metasurface reflector. In particular, the arbitrary manipulation can be unanimously predicted and concluded by our three-dimensional impedance-governed generalized Snells law of reflection (3D IGSL), which is rigorously derived from Greens functions and integral equations. Consequently, the vibrations of the extraordinary reflection and the incidence will form a spatial angle in between, rather than sitting in one plane. Such an inhomogeneous flat metasurface can be effectuated by means of impedance discontinuity, and further implemented

by tube arrays with properly designed lengths. Finite-element-simulation results agree with the theoretical prediction by 3D IGSL.

3.1 Out-of-incident-plane vibration of fluid particles

The coordinate is illustrated in Figure 3.1, where the flat metasurface reflector is placed at $z = 0$ plane, i.e., x-y plane. In water (speed of sound $c_0 = 1500m/s$; density $\rho_w = 1000kg/m^3$), an acoustic plane wave p_i from the space $z > 0$ is impinged upon the flat surface $z = 0$ with unit amplitude and the frequency $\omega = 3 \times 10^5$ rad/s. Figure 3.1(a-d) are the simulated acoustic fields in the upper space $z > 0$, which are the projections upon the plane perpendicular to z axis. For the incident field in Figure 3.1(a), one can notice that the vibrational direction of fluid particles (orange double-headed arrow) excited by the incidence forms the incident plane (yellow dashed line) with z axis. As shown in Figure 3.1(b) for the reflected field, if the impedance reflector is homogeneous, the particle vibration excited by the ordinary reflection p_{ro} (orange double-headed arrow) will be co-planar with the incident vibration, as expected intuitively.

In order to steer the acoustic vibrations freely, a metasurface reflector composed of the inhomogeneous specific acoustic impedance SAI, which can be realized by different layouts of tube resonators with designed lengths, is implemented in Figure 3.1(c,d), while the same incidence in Figure 3.1(a) is used. The incident plane (yellow dashed line) is identical throughout all cases in Figs. 1(a-d). It can be seen from the reflected fields in Figure 3.1(c,d) that the particle vibration excited by the reflection (blue

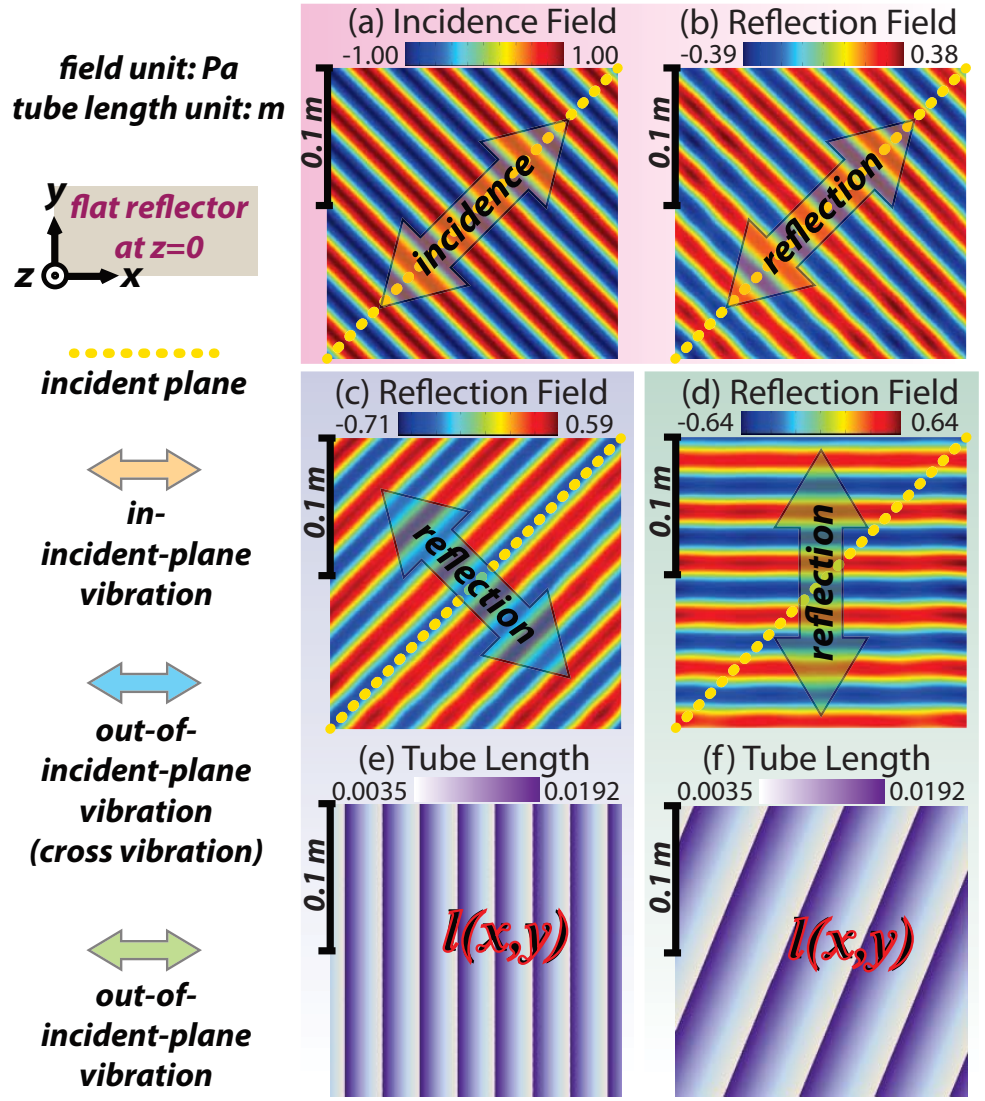

FIGURE 3.1: (a) Observing along $-\mathbf{z}$, an plane wave is propagating toward the metasurface at $z = 0$. The vibration of fluid particles excited by the incidence (orange double-headed arrow) is within the incidence plane (yellow dashed line). (b) The ordinary reflection generated by a homogeneous flat reflector excites the in-incident-plane particle vibration. (c) Observing along $-\mathbf{z}$, the flat metasurface reflector excites the out-of-incident-plane cross vibration of fluid particles (blue double-headed arrow). (d) Another metasurface reflector excites the extraordinary vibration of fluid particles (green double-headed arrow). (e,f) The realization schematics of the metasurface, and the tube lengths corresponding to (c) and (d) respectively are exhibited in (e,f). Figure adopted and reproduced with permission from ref. [51].

double-headed arrow) deviates away from the incident plane by employing the inhomogeneous impedance surface. Observing along $-\mathbf{z}$, we manipulate the x-y plane projection of the vibration (excited by reflection) perpendicular to the incident plane as shown in Figure 3.1(c), as named cross vibration. Another example is shown in Figure 3.1(d), where the out-of-incident-plane vibrational orientation (green double-headed arrow) is steered robustly by the flat metasurface at $z = 0$. The corresponding reflected acoustic field at $z > 0$ projected in the x-y plane is shown in Figure 3.1(d), verifying the robust and precise manipulation of the out-of-incident-plane vibrational orientations of fluid particles.

In order to provide a theoretical and systematic framework for precisely manipulating the vibrational orientation in fluids, we thereby establish 3D IGSL. Here we consider the reflection by a flat acoustic metasurface at $z = 0$, and formulate the modified Snells law in acoustics for inhomogeneous two-dimensional SAI [42]. More specifically, the inhomogeneous SAI will give rise to the out-of-incident-plane vibration excited by the extraordinary reflection p_{re} (uniquely controlled by 3D IGSL) as well as the in-incident-plane vibration excited by an ordinary reflection p_{ro}, as shown in Figure 3.2(a).

Interestingly, it is found that the acoustic metasurface at $z = 0$ designed according to 3D IGSL cannot alter the direction of p_{ro} excited by the metasurface reflector, but surprisingly can turn off p_{ro} as shown in Figure 3.2(b). In other words, our design can create the steerable p_{re} as well as the switchable p_{ro}. This is unique for our acoustic metasurface while it is generally difficult to eliminate the parasitic ordinary refraction or reflection for electromagnetic metasurfaces [1]. p_{re} can be in principle steered along arbitrary

directions by the acoustic metasurface, simultaneously with p_{ro} eliminated, resulting in the corresponding manipulation of cross vibration in the absence of the ordinary in-plane vibration. Therefore, 3D IGSL describes the generalized reflection law regarding the acoustic metasurface of 2D inhomogeneous acoustic impedance, and provides a clear-cut way for manipulating p_{re} and its vibration along arbitrary spatial angles.

Physically, our realization of our-of-plane vibration in fluids is based on the reference of the incident plane. Because the reflection plane is rotated by our design method, the vibration of acoustic reflected waves is out of the incident plane, but still within the reflection plane. This pseudo transverse polarization in fluids is different from the authentic transverse vibration for acoustic waves in solids or electromagnetic waves.

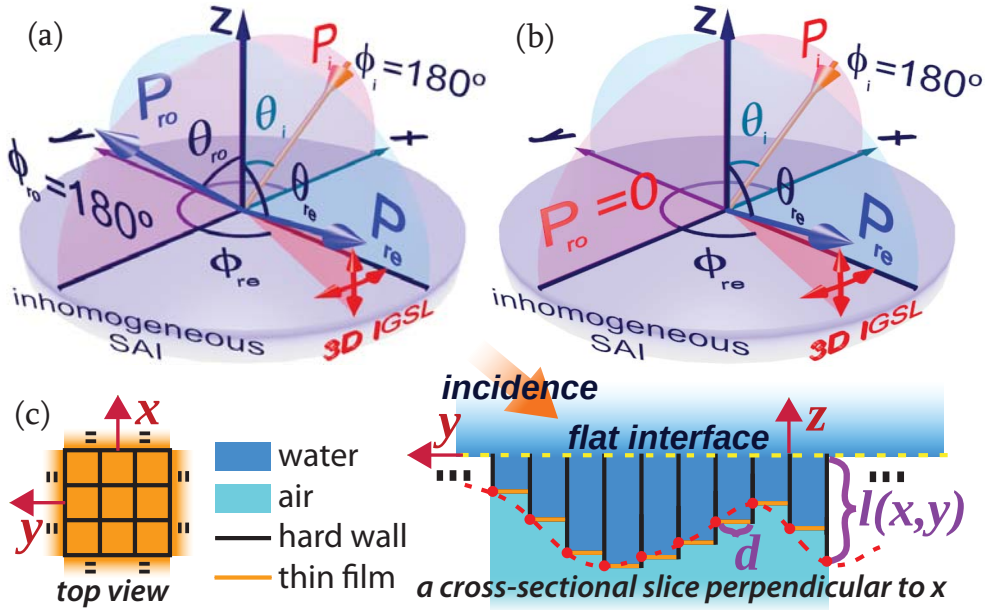

FIGURE 3.2: (a) For a flat metasurface reflector with an inhomogeneous 2D SAI, the directions of p_{ro}, i.e., θ_{ro} and ϕ_{ro}, are not influenced, while p_{re} occurs simultaneously with the direction θ_{re} and ϕ_{re} controlled by 3D IGSL. (b) If a heterogeneous SAI is properly designed upon the reflector, p_{ro} will become null. (c) Realization schematics by tube arrays, comprising the reflector (yellow dashed line). Figure adopted and reproduced with permission from ref. [51].

3.2 Two-dimensional varying metasurface

Here, we will focus on the theoretical formulation. As depicted in Figure 3.2(a,b), p_i, θ_i (the angle between the orange line and $\mathbf{z}$) and ϕ_i (the angle between $\mathbf{x}$ and the x-y-plane projection of the orange vector) stand for the incident plane wave, the incident polar angle and the azimuth angle, respectively. The similar notations are adopted for p_{ro} and p_{re}.

The inhomogeneous 2D SAI Z_n of the flat metasurface at $z = 0$ is the extension of the one-dimensional SAI that only creates the in-incident-plane vibration and redirection in acoustics, which was introduced in Chapter 2 [41]. For simplicity in modeling, we consider

$$Z_n(x, y, \omega) = A\left[1 - i\tan\frac{\psi(x, y)}{2}\right], \tag{3.1}$$

where A is an arbitrary real constant and $\psi(x, y)$ represents the spatially varying component only existing at the imaginary part. Note that $\psi(x, y)$ in Equation (3.1) has already taken into account the circular frequency.

We assume p_i in the upper space satisfies

$$p_i(x, y, z, \omega) = p_{i0}(\omega)\exp\left[ik_0(x\sin\theta_i\cos\phi_i + y\sin\theta_i\sin\phi_i - z\cos\theta_i)\right], \tag{3.2}$$

where k_0 stands for the wave number in free space and p_{i0} for the amplitude of the incidence. It is found that p_{ro} excited by the reflector at $z = 0$ with Z_n satisfies [41]

$$p_{ro}(x,y,z,\omega) = p_{i0}(\omega) \times \frac{2A\cos\theta_i - \rho_w c_0}{2A\cos\theta_i + \rho_w c_0} \times \exp\left[ik_0(x\sin\theta_{ro}\cos\phi_{ro} + y\sin\theta_{ro}\sin\phi_{ro} + z\cos\theta_{ro})\right], \tag{3.3}$$

where ρ_w, c_0 are the density and the speed of sound in the upper space $z > 0$ in Figure 3.2(a-b), $\theta_{ro} = \theta_i$ and $\phi_{ro} = \phi_i$. p_{ro} is attributed to the reflection by the properly-averaged value of the inhomogeneous 2D SAI Equation (3.1), while the variance of the 2D SAI is the cause of p_{re} [41]. Here, by virtue of Greens functions [41, 52], p_{re} in the upper space, serving as the result of the 2D SAI variation, can be expressed as an integral equation:

$$p_{re}(x,y,z,\omega) = ik_0\frac{\rho_w c_0}{2A} \times \int_{-\infty}^{\infty} dy_0 \int_{-\infty}^{\infty} dx_0 e^{i\psi(x_0,y_0)}[p_i(x_0,y_0,0,\omega) + p_{ro}(x_0,y_0,0,\omega) + p_{re}(x_0,y_0,0,\omega)]G(x,y,z,\omega;x_0,y_0,0), \tag{3.4}$$

where G stands for the Greens function accommodating the boundary condition. In the far field approximation [53], G can be derived explicitly:

$$G(\mathbf{r},\omega;\mathbf{r}_0) = \frac{\exp(ik_0|\mathbf{r}|)}{4\pi|\mathbf{r}|} \times \exp[-ik_0(x_0\sin\theta_{re}\cos\phi_{re} + y_0\sin\theta_{re}\sin\phi_{re})] \times [\exp(-ik_0 z_0\cos\theta_{re}) + \frac{2A\cos\theta^* - \rho_w c_0}{2A\cos\theta^* + \rho_w c_0}\exp(ik_0 z_0\cos\theta_{re})], \tag{3.5}$$

where $\mathbf{r} = (x,y,z)$, $\mathbf{r}_0 = (x_0,y_0,z_0)$, and θ^*, a constant, describes the effective incident angle with respect to the Greens function Equation (3.5) [54]. Inserting Equation (3.5) into Equation (3.4) and using Born approximation [55], we are able to determine p_{re}, which includes the following term:

$$p_{re} \propto \int_{-\infty}^{\infty} dy \int_{-\infty}^{\infty} dx \times e^{i\psi(x,y)} \exp[ik_0 x(\sin\theta_i \cos\phi_i - \sin\theta_{re}\cos\phi_{re}) + ik_0 y(\sin\theta_i \sin\phi_i - \sin\theta_{re}\sin\phi_{re})]. \tag{3.6}$$

Note that for the trivial case when $\psi(x, y) = 0$, Equation (3.6) is non-zero which implies that p_{re} propagates along the same direction as p_{ro}. That is to say, if the flat metasurface is of uniform SAI which only generates the common reflection, the contribution of Equation (3.6) should also be taken into account besides Equation (3.3). In addition, we find that Equation (3.6) is a two-dimensional Dirac Delta when $\psi(x, y)$ is a linear function with respect to x and y, which imposes the directivity of p_{re} to be:

$$\Psi(\theta_{re}, \phi_{re}) \propto \delta[k_0 x(\sin\theta_i \cos\phi_i - \sin\theta_{re}\cos\phi_{re}) + k_0 y(\sin\theta_i \sin\phi_i - \sin\theta_{re}\sin\phi_{re}) + \psi(x, y)]. \tag{3.7}$$

Therefore, the spatial directivity of p_{re} only makes sense when

$$\begin{cases} \sin\theta_{re}\cos\phi_{re} - \sin\theta_i \cos\phi_i = \frac{1}{k_0}\frac{\partial\psi(x,y)}{\partial x} \\ \sin\theta_{re}\sin\phi_{re} - \sin\theta_i \sin\phi_i = \frac{1}{k_0}\frac{\partial\psi(x,y)}{\partial y} \end{cases}, \tag{3.8}$$

where ψ is a linear function with respect to x and y. Equation (3.8) unveils the relation between the incident direction and the direction of p_{re}, i.e., 3D IGSL, which is regarded as the generalized law for acoustic metasurface reflection. We note that if the metasurface is thin and allows transmission, Equation (3.8) is the generalized law of refraction for the metasurface as well, revealing the generality of our approach. It is noteworthy that if ψ

is a constant for a uniform 2D SAI, Equation (3.8) will be reduced to the usual Snells law. 3D IGSL serves the manipulation of the vibration of fluid particles excited by p_{re}, theoretically via tuning the parameter ψ of the inhomogeneous SAI flat reflector, with no influence on the direction of p_{ro}, as illustrated in Figure 3.2(a).

Other advantage of our Green's function formulation also gives p_{ro} amplitude as [41]

$$r_{ro} = p_{i0}(\omega) \times (2A\cos\theta_i - \rho_w c_0)/(2A\cos\theta_i + \rho_w c_0). \tag{3.9}$$

Usually, both p_{ro} and p_{re} coexist, but 3D IGSL only tunes θ_{re} and ϕ_{re}. In order to obtain purely cross vibration excited by p_{re} with full control, we need to eliminate p_{ro}. By particularly controlling the value of A in Equation (3.1), we manage to switch off p_{ro}, as illustrated in Figure 3.2(b). Based on Equation (3.9), if $A = (\rho_w c_0)/(2\cos\theta_i)$, p_{ro} will be eliminated, while the 2D SAI becomes

$$Z_n(x, y, \omega) = \frac{\rho_w c_0}{2\cos\theta_i}\left[1 - i\tan\frac{\psi(x, y)}{2}\right]. \tag{3.10}$$

Thus, it is discovered that metasurface cannot affect the direction of p_{ro} but just keep or eliminate p_{ro}.

Equally important is the plausible realization schematic of the inhomogeneous SAI in Equation (3.1), implemented by discretized impedance. As depicted in Figure 3.2(c), all hard-sidewall tubes are assembled and juxtaposed perpendicular to the flat interface, illustrated in the top view. Each tube, serving as one discrete 2D SAI pixel of the flat metasurface reflector,

has a square cross section whose width is d, with four surrounding hard sidewalls (black). In the view of a cross-sectional slice in Figure 3.2(c), one end of each tube constitutes the flat interface of the metasurface at $z = 0$ (yellow dashed line), and the other end contacts with air (light blue). The space $z > 0$ and the interior are filled with water (dark blue), without separation. The water-air interface separated by a thin film (orange) is regarded as the pressure-release termination of each tube.

In order to realize the 2D SAI inhomogeneity by discretized impedance, $d < 2\pi/k_0$ is required to eliminate higher diffraction orders. The SAI of each tube at the opening facing $z > 0$ can be calculated [42]:

$$Z_t(x, y, \omega) \approx \frac{\rho_w c_0 {k_0}^2 d^2}{2\pi} - i\rho_w c_0 \tan\left[k_0 l(x, y) + k_0 \Delta l\right], \tag{3.11}$$

where $l(x, y)$ is the spatial distribution of the length of each tube and $\Delta l \approx 0.6133 d/\sqrt{\pi}$ is the effective end correction. By comparison between Equation (3.1) and Equation (3.11), it is required that $A = \rho_w c_0 {k_0}^2 d^2/(2\pi)$ and $A \tan[\psi(x, y)/2] = \rho_w c_0 \tan\left[k_0 l(x, y) + k_0 \Delta l\right]$, leading to the value of the discretized spacing d and the dependence between $l(x, y)$ and $\psi(x, y)$:

$$\begin{aligned} d &= \sqrt{(2\pi A)/(\rho_w c_0 {k_0}^2)} \\ l(x, y) &= \tfrac{1}{k_0} \arctan[\tfrac{{k_0}^2 d^2}{2\pi} \tan \tfrac{\psi(x,y)}{2}] + \tfrac{n\pi}{k_0} - \Delta l \end{aligned} \tag{3.12}$$

where the arbitrary integer n is required to be set suitably to make l a positive value. Thus, the change of ψ at the flat-metasurface reflector, representing the manipulation of fluid-particle vibrations through the control of p_{re}, is now interpreted by the change of l [red dashed line in Figure 3.2(c)], demonstrating one straightforward realization scheme based on impedance

discontinuity. In principle, tubes can be regarded as Helmholtz resonators, and the complex SAI at each pixel can thus be realized by a suitable arrangement of resonators.

3.3 Three-dimensional control of extraordinary reflection

The simulation results verify the robustness in the manipulation of fluid-particle vibrations according to our 3D IGSL. We first consider the ideal case without using the tube-array configuration, by selecting water as the background media and $\psi(x, y) = -100\sqrt{3}y$ at the SAI metasurface in Equation (3.10). The incident plane ultrasound with $\omega = 3 \times 10^5$ rad/s, $\theta_i = 18°$ and $\varphi_i = 180°$ is impinged upon the metasurface at $z = 0$. The spatial angles for p_{re}, i.e., θ_{re} and φ_{re}, are theoretically found to be 66.9° and 250.4° by 3D IGSL in Equation (3.8), respectively. The simulation in Figure 3.3(b) validates our theory, where p_{ro} disappears thoroughly owing to the specific design of the coefficient according to Equation (3.10). The cut slice at $\varphi_{re} = 250.4°$ in Figure 3.3(b) clearly shows that p_{re} is propagating towards the predicted direction without any disturbance. In other words, we realize this out-of-incident-plane reflection, and simultaneously achieve the full manipulation of its fluid-particle vibration.

In particular, in Figure 3.3(a), the same parameters are kept except for another selection for A, whose value is arbitrarily taken to be $\rho_w c_0$. It clearly shows that p_{ro} coexists and interferes with p_{re}, but p_{re} still keeps the same direction ($\theta_{re} = 66.9°$ and $\varphi_{re} = 250.4°$), verifying our theoretical prediction. Although such double reflections are predictable well by our

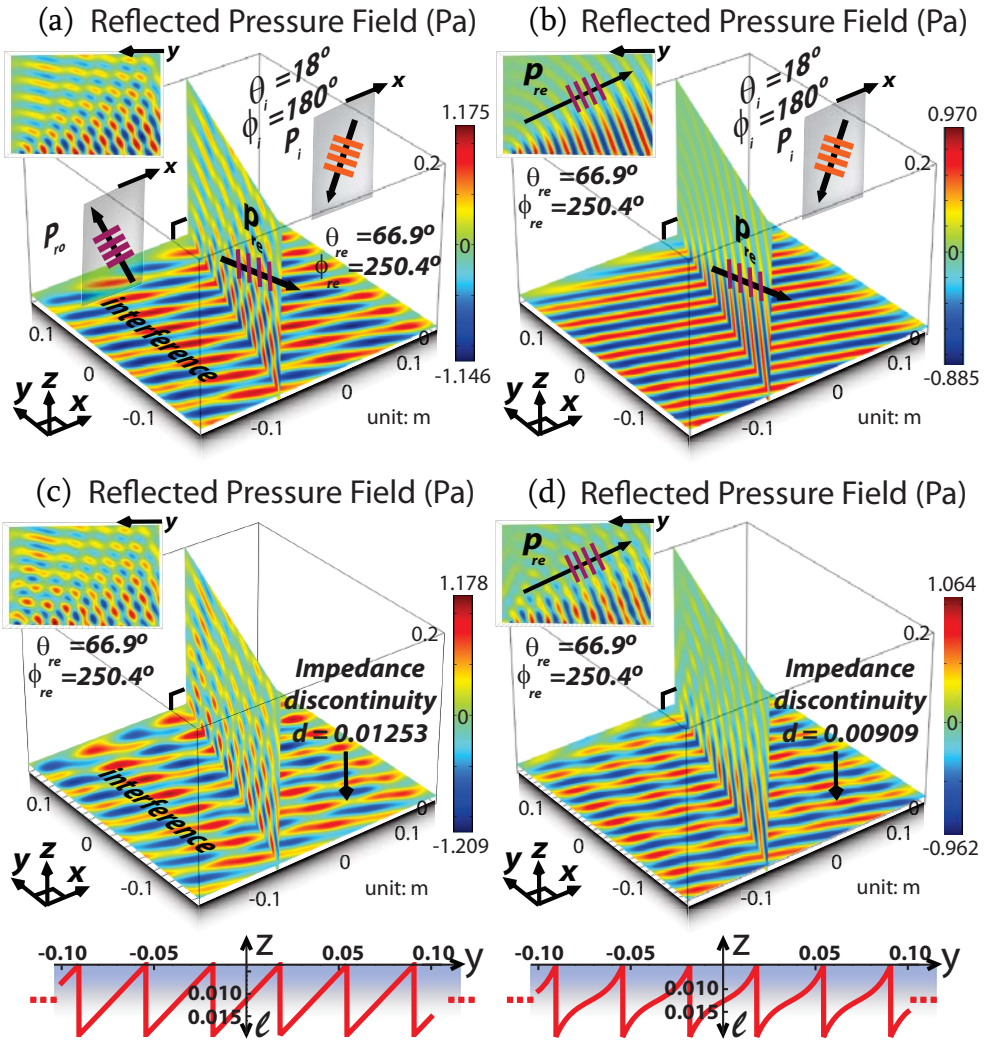

FIGURE 3.3: (a) The acoustically flat-metasurface reflector with an inhomogeneous SAI excites both p_{ro} and p_{re} when an arbitrary A is chosen in Equation (3.1). The fluctuation of the interference verifies our theory. (b) A particular SAI is suggested according to Equation (3.10) so that only the pure out-of-incident-plane vibration is excited by p_{re} with an expected direction. (c,d) Simulation results based on the realization of tube arrays with relations $l(x, y)$ enclosed below, corresponding to the cases (a) and (b) respectively. Figure adopted and reproduced with permission from ref. [51].

theory, p_{ro} will disturb the manipulated out-of-incident-plane fluid-particle vibration excited by p_{re} in Figure 3.3(a). Therefore, we generally switch off p_{ro} and make the out-of-incident-plane vibration excited by p_{re} pure, as demonstrated in Figure 3.3(b).

Next, we consider the realization when the metasurface reflector with realistic discretized impedance is applied, in order to reproduce Figure 3.3(a,b). In the reflected-field simulation of Figure 3.3(c,d), $d = 0.01253$ and $d = 0.00909$ are selected respectively according to Equation (3.12), and their corresponding distributions of $l(x, y)$ are enclosed. (In these two cases there is no variation of l along $\mathbf{x}$.) Figure 3.3(c) shows strong interference between p_{re} and p_{ro}, while Figure 3.3(d) shows the nearly undisturbed p_{re}, coinciding with Figures 3.3(a) and 3(b), respectively, verifying our proposed realization using the layout of tube arrays.

Recalling the given example in Figure 3.1, we set the oblique incident angles as $\theta_i = 60°$ and $\varphi_i = 225°$. The flat acoustic metasurface with $\psi(x, y) = 100\sqrt{6}x$ in Equation (3.10) is placed as the reflector at $z = 0$, whose tube-length distribution $l(x, y)$ is illustrated in Figure 3.1(e) according to Equation (3.12). Through 3D IGSL in Equation (3.8), we manage to make p_{re} arise with the direction $\theta_{re} = 60°$ and $\varphi_{re} = -45°$, and simultaneously make p_{ro} eliminated, corresponding to the simulation of the reflected field in Figure 3.1(c). The perpendicular intersection between the incident plane and the x-y-plane projection of the particle vibrations in Figure 3.1(c) exhibits the so-called cross vibration of fluid particles excited by reflection, leading to this intriguing tweak of vibrational orientations in fluids. Figure 3.1(d) is another example to verify the robustness of our theory. The flat metasurface reflector with $\psi(x, y) = 50\sqrt{6}x - 100\sqrt{3}y + 50\sqrt{6}y$

in Equation (3.10) is selected and the corresponding $l(x, y)$ is illustrated in Figure 3.1(f). Similarly, by the prediction from 3D IGSL, p_{re} occurs to the direction $\theta_{re} = 60°$ and $\varphi_{re} = 270°$ with the suppression of p_{ro}, whose field projection at the plane perpendicular to $\mathbf{z}$ is Figure 3.1(d).

3.4 Conclusion

In conclusion, we propose an acoustic flat metasurface reflector to manipulate vibrational orientations of fluid particles in acoustics, and show that a complete conversion between two perpendicular vibrations by deviating the extraordinary reflection out of the incident plane. It is found that the control of the metasurface parameter can keep the extraordinary reflection only, while suppressing the ordinary reflection. We also theoretically unveil the generalized rule of three-dimensional impedance-governed generalized Snell's law of reflection with respect to the specific acoustic impedance. The out-of-incident-plane fluid-particle vibration and the arbitrary degree of freedom in directional manipulation are numerically implemented using the designed layout of tube arrays.

Chapter 4

Manipulating acoustic focus with an active metasurface piezoelectric transducer

This chapter establishes the prototype of acoustic metasurface piezoelectric transducer (PT), whose piezoelectric elements are squeezed into a flat thin layer compared to the scale of the entire device. The active planar interface also extends the knowledge of acoustic metasurface engineering for the deflection of sound beams using passive elements [49, 51]. Through the optimized ring configurations of the active metasurface PT, we are able to manipulate the focal pattern and the focal resolution in acoustic far fields. Firstly, we design the far-field finite-length focal needle with the manipulated distance and depth. Its focal resolution is subwavelength for the full width at half maximum (FWHM), and it propagates without divergence for a distance of 5.9λ as designed, longer than the depth 4λ of the reported optical needle [56]. These two designed focusing properties created

with PTs were never achieved in acoustics, to the best of our knowledge. To further verify the robustness of our manipulation of the focal pattern, via another optimized ring configuration, we obtain the designed far-field multiple foci, whose FWHM (0.45λ) beats the Rayleigh diffraction limit of conventional acoustic instruments (0.5λ). Besides, to demonstrate the manipulation of the focal resolution, we design the extreme case of the super-oscillatory super resolution, whose size is 0.3λ in acoustic far fields, much smaller than the diffraction limit.

4.1 Design of planar metasurface piezoelectric transducer

In the 3D view of the configurable planar metasurface PT prototype in Figure 4.1(a), piezoelectric rings (red) are unevenly spaced with hard-boundary mask rings (blue) in between. A type of common artificial ceramic is employed as the piezoelectric material: lead zirconate titanate PZT-5H [57]. In the radial view, the thickness q is set identical for all PZT-5H rings, and the ring configuration ($r1$, $rr1$, $r2$, $rr2$, $\cdots$) will be optimized according to different focusing manipulation. The thin hard-boundary mask rings in between, through which no sound can pass, are the complements of the spaced gaps between PZT-5H rings, co-planar with $z = 0$. The entire PT is axisymmetric with respect to $+\mathbf{z}$, and the upper surface of the structure at $z = 0$ can be regarded as a flat active metasurface according to the radial cross-sectional view. In our following demonstrations in air (density: $\rho_a = 1.21kg/m^3$; speed of sound: $c_0 = 343m/s$), we will show the designed focal pattern and the focal resolution created with the PT prototype in

acoustic far fields, the simulation of which is carried out by the finite element method (FEM). In detail, COMSOL Multiphysics is the platform we use, and the simulation is facilitated by the coupling of the embedded acoustic module and the acoustic-piezoelectric interaction module concurrently.

The design method and the related physics are elaborated in this part. The electromechanical constitutive equations governing the piezoelectric effect of PZT-5H are written in the stress-charge form [59]:

$$\mathbf{T} = c_E\mathbf{S} - e^T\mathbf{E};\ \mathbf{D} = e\mathbf{S} + \varepsilon_S\mathbf{E}, \tag{4.1}$$

where $\mathbf{T}$ and $\mathbf{S}$ are the vectors of stress and strain; $\mathbf{E} = -\nabla\phi$ is the electric field, which is rephrased with the electric potential ϕ exerted on the PZT-5H rings; c_E the elasticity matrix evaluated at a constant electric field; e the coupling matrix; $\mathbf{D}$ the electric displacement; ε_S the electric permittivity matrix evaluated at a constant mechanical strain. Usually, c_E is straightforwardly given as an anisotropic symmetric matrix; $\varepsilon_S = \varepsilon_0\varepsilon_{Sr}$ includes the relative permittivity matrix ε_{Sr}. These parameters of PZT-5H are listed in Appendix C. For each PZT-5H ring whose poling direction is aligned toward $+\mathbf{z}$, the boundary conditions (B.C.s) are indicated in Figure 4.1(b). The structural B.C.s for the inner and the outer sides are free of constraint, while the bottom is fixed with the structural displacement $\mathbf{u} = 0$. The top undergoes the interaction between sounds and structures [59]:

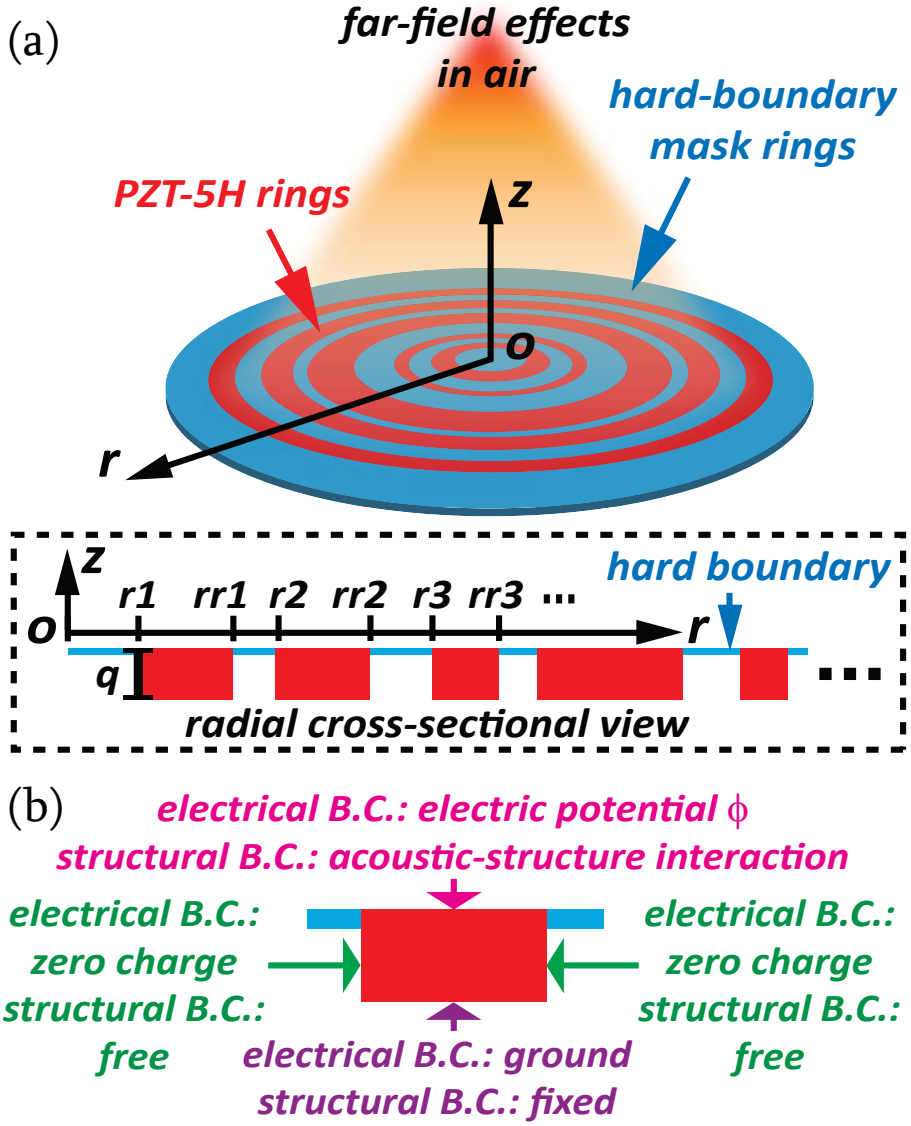

FIGURE 4.1: (a) Schematics of the configurable planar metasurface PT prototype. Inside the dashed box is the radial cross-sectional view of the ring configuration, showing the unevenly-distributed piezoelectric elements and the hard boundaries. (b) The boundary condition of each piezoelectric ring observed from the radial cross-sectional view. Figure adopted and reproduced with permission from ref. [58].

$$\begin{aligned}
&\overline{\overline{\mathbf{T}}} \cdot \mathbf{n}_S \Big|_{z=0} = -\mathbf{n}_S p|_{z=0} \\
&\mathbf{n}_S \cdot \left(-\tfrac{1}{\rho_0}\nabla p\right)\Big|_{z=0} = \mathbf{n}_S \cdot \tfrac{\partial^2 \mathbf{u}}{\partial t^2}\Big|_{z=0} \\
&\overline{\overline{\mathbf{S}}} = \tfrac{1}{2}\left[(\nabla \mathbf{u})^T + \nabla \mathbf{u}\right]
\end{aligned} \tag{4.2}$$

where $\overline{\overline{\mathbf{T}}}$ and $\overline{\overline{\mathbf{S}}}$ are the tensors of stress and strain; $\mathbf{n}_S$ is the outward-pointing unit normal vector seen from inside PZT-5H. Briefly, the first equality indicates the acoustic pressure load p; the second makes the normal acceleration of p on the boundary $z = 0$ equal to that of the structural displacement; the third is the intrinsic constitutive equation of $\overline{\overline{\mathbf{S}}}$ and $\mathbf{u}$ inside solids. Meanwhile, the electrical B.C.s for the inner and the outer sides are free of charge $\mathbf{n}_S \cdot \mathbf{D} = 0$, whilst the bottom touches ground $\phi = 0$. The top is assigned with monochromatic $\phi = V_0 \cos(2\pi f t)$. One common technique to impose the voltage bias is a sandwiched structure with PTH-5H elements between two Au electrode layers.

Next, in order to manipulate the far-field focal pattern or the focal resolution created with the planar metasurface PT prototype, we propose the acoustic Rayleigh-Sommerfeld diffraction integral (RSI) in conjunction with the method of binary particle swarm optimization (BPSO) [60–62]. The derivation starts from the Kirchhoff-Helmholtz integral [42]:

$$\iint_S dS' \left[p(\mathbf{r}', \omega)\nabla' g(|\mathbf{r} - \mathbf{r}'|) - g(|\mathbf{r} - \mathbf{r}'|)\nabla' p(\mathbf{r}', \omega)\right] \cdot \mathbf{n}' = p(\mathbf{r}, \omega), \tag{4.3}$$

where $\mathbf{r} \in \Omega$, $g(x) = \exp(ik_0 x)/(4\pi x)$ and $k_0 = 2\pi f/c_0$. $p(\cdot)$ and $g(\cdot)$ are monochromatic wave functions defined throughout the domain Ω bounded by a closed surface S, while $\mathbf{n}' \cdot \nabla'$ denotes the differentiation along the inward normal to S. Provided that Ω is the half space $z \geq 0$,

S thus consists of the plane $z = 0$ and a hemisphere of infinite radius, centered at the origin. After adopting the Sommerfeld radiation condition $\lim_{r\to\infty} [\partial p(\mathbf{r},\omega)/\partial r \ - ik_0 p(\mathbf{r},\omega)] = 0$ to Equation (4.3), we obtain:

$$\frac{1}{4\pi}\iint_{z'=0} dx'dy'[p(\mathbf{r}',\omega)\frac{\partial}{\partial z'}\frac{\exp(ik_0R_1)}{R_1} - \frac{\exp(ik_0R_1)}{R_1}\frac{\partial p(\mathbf{r}',\omega)}{\partial z'}] = p(\mathbf{r},\omega), \tag{4.4}$$

where $R_1 = \sqrt{(x-x')^2 + (y-y')^2 + (z-z')^2}, z > 0$. On the other hand, if $\mathbf{r}$ situates in the lower half space $z < 0$, we will obtain [11]:

$$\frac{1}{4\pi}\iint_{z'=0} dx'dy'[p(\mathbf{r}',\omega)\frac{\partial}{\partial z'}\frac{\exp(ik_0R_2)}{R_2} - \frac{\exp(ik_0R_2)}{R_2}\frac{\partial p(\mathbf{r}',\omega)}{\partial z'}] = 0, \tag{4.5}$$

where $R_2 = \sqrt{(x-x')^2 + (y-y')^2 + (z+z')^2}, z < 0$. Subsequently, making use of the connection between R_1 and R_2 at $z = 0$, we incorporate Equation (4.4) and Equation (4.5), bringing about the acoustic RSI:

$$p(\mathbf{r},\omega) = \frac{1}{2\pi}\iint_{z'=0} p(\mathbf{r}',\omega)\frac{\partial}{\partial z'}\frac{\exp(ik_0R_1)}{R_1}dx'dy'. \tag{4.6}$$

Applying the first-order Born approximation [55] to Equation (4.6), which simplifies the vibration at the fluid-solid interfaces at $z = 0$ to be uniform and binary, we finalize the equation as the acoustic RSI cum BPSO:

$$|p(\mathbf{r},\omega)|^2 = \left|\frac{1}{2\pi}\iint_{z'=0} p_{uni}(\mathbf{r}',\omega)\frac{z\exp(ik_0R_1)}{{R_1}^2}\left(ik_0 - \frac{1}{R_1}\right)dx'dy'\right|^2, \tag{4.7}$$

where $p_{uni}(\cdot)$ is a binary function describing the ring configuration at $z = 0$, optimized for the designed focal pattern or focal resolution $|p(\mathbf{r},\omega)|^2$. Other

than the requirement of acoustic pressure as well as its normal derivative in Equation (4.3), Equation (4.7) only requires the acoustic pressure on the surface, suitably for BPSO.

In general, BPSO is a nature-inspired evolutionary algorithm for stochastic optimization [62]. At first, the designed energy distribution $|p(\mathbf{r},\omega)|^2$ will be preset to benchmark acoustic focal patterns or resolutions in respective scenarios. Simultaneously, by means of Equation (4.7), BPSO will be implemented to optimize the parameter $\mathbf{r} = [r_1, r_2, r_3, ..., r_N]$ in order to fulfill the benchmark $|p(\mathbf{r},\omega)|^2$. For simplicity, the ring width Δr of the planar metasurface PT is fixed in our design. Once $\mathbf{r}$ is given, one can obtain another parameter $\mathbf{rr} = [rr_1, rr_2, rr_3, ..., rr_N]$ by $\mathbf{rr} = \mathbf{r} + \Delta r$. Then, the parameters $\mathbf{r}$ and $\mathbf{rr}$ determine the ring configuration in Figure 4.1(a). Although the fixed Δr sets a constraint in designing the active metasurface PT, this low-cost approach always works well in many applications [63], as we will show later.

4.2 Generation of an acoustic focal needle

To vindicate the proposed method, i.e. the acoustic RSI cum BPSO, in the manipulation of acoustic focusing, we first demonstrate the manipulation of the acoustic focal patterns such as the designed focal needle and the designed multiple foci. The arbitrary design of a focal pattern is impossible if we simply resort to acoustic wavefront construction by the method of effective medium [43]. In our case for the pattern of a finite-length focal needle on axis, we conveniently select $V_0 = 5V$ and $f = 100kHz$ that generates acoustic waves of $\lambda = 3.43mm$ in the space $z > 0$. Note that

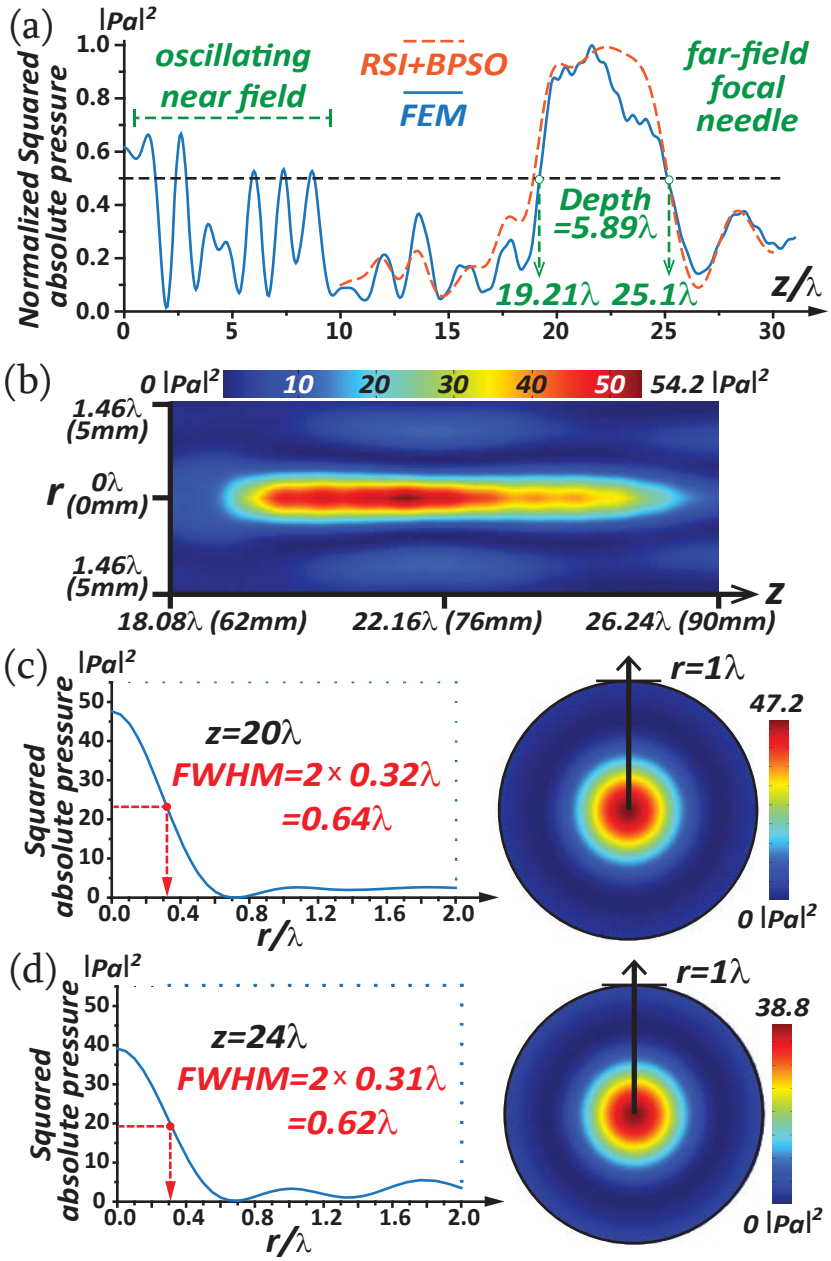

FIGURE 4.2: (a) The normalized squared absolute pressure, displaying the pattern of the designed finite-length far-field focal needle. (b) The field distribution of the squared absolute pressure around the focal needle. (c,d) The radial distributions of the squared absolute pressure at the cross sections $z = 20\lambda$ and $z = 24\lambda$, with their respective field distributions. Figure adopted and reproduced with permission from ref. [58].

for the purpose of a finite-length focal-needle pattern in the far field, we require a depth of continuous acoustic focal energy along the axis with the low energy level at the rest, whilst the location, i.e., both the depth of the needle and the specific positions of the two ends away from the transducer, could be subtly designed as well. In Figure 4.2(a), the on-axis focal-needle pattern, whose position is preset to extend from 19.2λ to 25.1λ, is designed as the orange dashed curve $|p(\mathbf{r},\omega)|^2$, while simultaneously the optimized ring configuration is calculated by the acoustic RSI cum BPSO as described above. The optimized ring configuration listed in Appendix C includes 30 PZT-5H rings with the maximum radius of ∼180 mm, while q is adjusted optimally to be 4 mm.

In the same plot, the full-wave acoustic field generated by the planar and active metasurface PT as the real case is simulated by the FEM as the blue curve, using Equation (4.1) and Equation (4.2), and the result coincides with the designed finite-length focal-needle pattern (orange dashed curve). It is noteworthy that the standing-wave-like oscillation from 0λ to $\sim 10\lambda$ along $\mathbf{z}$ direction agrees with the classic characteristic of acoustic near fields [42]. Besides, we notice that most energy is focused into the designed far-field focal region from 19.21λ to 25.1λ, implying the focal needle of the depth 5.89λ as designed, longer than the depth $\sim 4\lambda$ of the reported optical needle [56]. In Figure 4.2(b), the field pattern of $|p(\mathbf{r},\omega)|^2$ simulated by FEM around the focal needle is displayed. The contrast between the intense needle and the ambient quiet field is apparent, which meets the requirement of the focal-needle shape.

It is necessary to mention the subwavelength focal resolution of the focal-needle pattern in Figure 4.2(c,d). The radial distributions of the squared

absolute pressure are plotted on the left while their field distributions are on the right. The FWHM of the focal size in the far field is measured to be $\sim 0.64\lambda$ at $z = 20\lambda$ and $z = 24\lambda$, smaller than one wavelength but larger than the diffraction limit. We may also conclude from Figure 4.2(c,d) that the acoustic needle pattern is formed of a nearly constant subwavelength width throughout. Moreover, the intensity of the side-lobes in Figure 4.2(c,d) is drastically smaller than the central intensity, crucially for potential imaging applications. Note that such subwavelength acoustic focusing is generated in the true far field without resorting to evanescent acoustic waves limited to the near field only.

4.3 Generation of acoustic far-field multiple foci

To further show the robustness of the acoustic-focusing manipulation, we take the example of the acoustic far-field multiple foci as another designed focal pattern. Here, the multiple foci are designed as the four discrete foci along the axis in the far field. The corresponding normalized energy pattern $|p(\mathbf{r}, \omega)|^2$ designed by the acoustic RSI cum BPSO is the orange dashed curve in Figure 4.3(a), using the ring configuration which is simultaneously optimized in this case. Note that the ring configuration here is designed and optimized in the same way except for a different focal pattern (benchmark). It includes 28 PZT-5H rings, whose parameters are listed in Appendix C. $q = 3mm$ is optimized here while V_0 and f remain the same. The blue curve indicates the full-wave simulation by FEM using

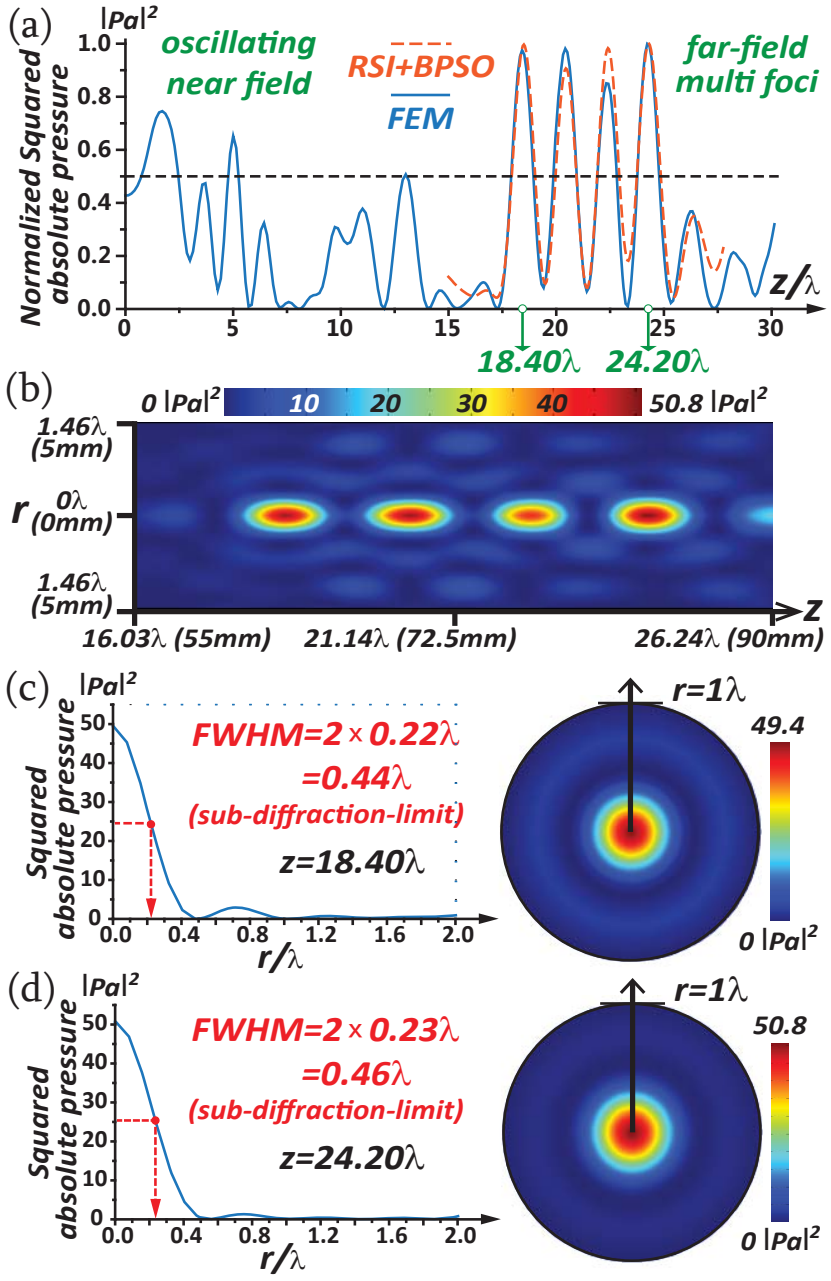

FIGURE 4.3: (a) The normalized squared absolute pressure, displaying the pattern of the designed far-field multiple foci. (b) The field distribution of the squared absolute pressure around the multiple foci. (c,d) The radial distributions of the squared absolute pressure at the cross sections $z = 18.4\lambda$ and $z = 24.2\lambda$, and their respective field distributions. Figure adopted and reproduced with permission from ref. [58].

Equation (4.1) and Equation (4.2). Again, the satisfactory agreement between these two outcomes confirms our pattern design. The corresponding field distribution in Figure 4.3(b) is simulated with respect to $|p(\mathbf{r},\omega)|^2$ around the multiple foci. Also, we notice that the focal resolution (FWHM $\sim 0.45\lambda$) of the multiple foci in Figure 4.3(c,d) is subwavelength and even beats the Rayleigh diffraction limit of 0.5λ, which was never realized in terms of PT technology.

As mentioned in the above two cases, by means of the properly-optimized ring configurations, we are able to achieve the designed acoustic focal patterns with a subwavelength resolution as well as a sub-diffraction-limit resolution. The underlying physics of achieving the focal resolution beyond the restriction of diffraction limit by means of the multiple-ring active metasurface transducer is the interference and the diffraction of excited sound beams.

In essence, Rayleigh diffraction has Airy pattern proportional to $J_1(k_r NA)$, where k_r is the radial wavenumber and NA is the numerical aperture. The pattern can be decomposed into $\propto [J_0(k_r NA) + J_2(k_r NA)]^2$ where the term $J_2(k_r NA)$ makes the focal size larger. In our case, each ring only generates $J_0(k_r NA)$ at the focal point. Therefore, by eliminating $J_2(k_r NA)$, the superposition at the focal plane breaches the traditional Rayleigh diffraction limit, while the algorithm BPSO simultaneously optimizes the ring configuration to further improve the acoustic focal resolution [63]. If we intend to further enhance the focal resolution to the deep sub-diffraction-limit focal size substantially smaller than 0.38λ, the situation will turn into the extreme case of the super-oscillatory super resolution [60, 61].

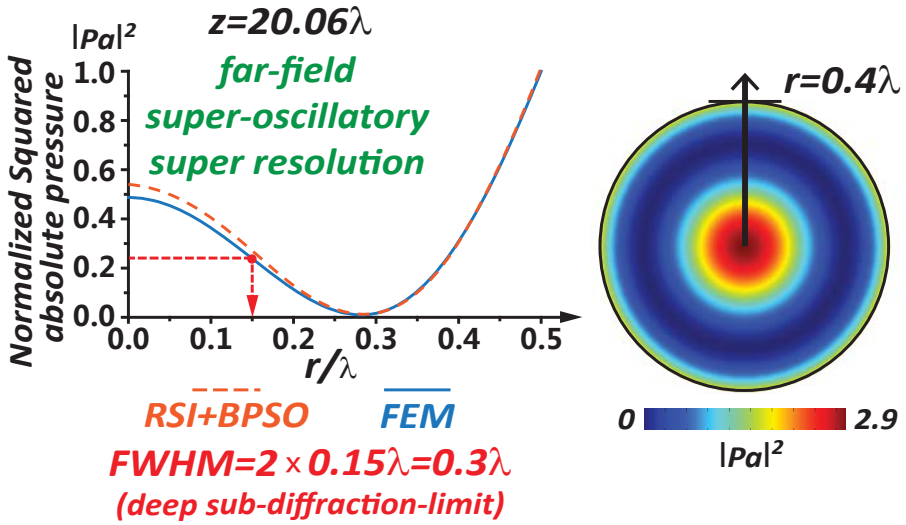

FIGURE 4.4: The radial distribution of the normalized squared absolute pressure at the cross section $z = 20.06\lambda$ on the left, showing the focal size of the far-field acoustic super-oscillatory super resolution. On the right is the corresponding field distribution of the squared absolute pressure.
Figure adopted and reproduced with permission from ref. [58].

4.4 Acoustic super-oscillatory super resolution

Our design method, the acoustic RSI cum BPSO in terms of PT technology, is able to manipulate the acoustic focal resolution as well and to increase it to acoustic super-oscillatory super resolution. Super oscillation is a sort of phenomenon associated with the fact that the band-limited functions can oscillate arbitrarily faster locally than the highest Fourier components, which makes it possible to break the diffraction limit and to reduce the focal size to be infinitesimal. In this case, we choose $V_0 = 100V$ and $f = 40kHz$ for the electric potential exerted on all PZT-5H rings, which produce acoustic waves of $\lambda = 8.575mm$ in air. After setting the acoustic super-oscillatory super resolution (FWHM $= 0.3\lambda$ at $z = 20.06\lambda$) as the designed focal resolution, we simultaneously optimize the ring configuration of the active metasurface PT in the same way, which includes 19 PZT-5H rings as shown in Appendix C, while $q = 2mm$ is adopted here optimally. The optimized result is the orange dashed curve in Figure 4.4, showing the designed radial distribution of the normalized $|p(\mathbf{r}, \omega)|^2$ at $z = 20.06\lambda$. The blue curve shows the corresponding full-wave simulation. The field distribution of the squared absolute pressure at the same cross section is plotted on the right in Figure 4.4 to exhibit the result of the focal-resolution manipulation.

We manage to control the focal size of the super-oscillatory super resolution to be 0.3λ in acoustic far fields, substantially smaller than 0.5λ. Nevertheless, if the FWHM of the focal spot is smaller than 0.38λ, there is an inevitable trade-off uniquely in terms of the super-oscillatory case, which

does not exist for a larger FWHM. Namely, the cost of the super-oscillatory super resolution is that most on-axis focal energy would be unavoidably squeezed away into the side-lobes as shown in Figure 4.4 [63]. In principle, the deep sub-diffraction-limit super resolution can be manipulated to be infinitesimal, but the sacrifice is the increasing side-lobes that make the super-oscillatory super resolution less efficient. However in spite of the naturally-inevitable trade-off in the super-oscillatory case, people also try applying it in biological imaging [60].

4.5 Discussion

Physically, the proposed active and configurable planar metasurface PT used for the manipulation of acoustic focusing is a sort of binary-amplitude exciter for directly focusing the excited sounds into a certain pattern or a designed resolution in the post-evanescent fields, by optimally modifying the constructive interference of a large amount of acoustic beams. The acoustic RSI cum BPSO is applied to optimize the ring configuration on the active metasurface after certain focusing targets such as focal patterns or focal resolutions are chosen. Additionally, the manipulation of acoustic focusing is not the translation from optics, whose binary mask is passive without energy feeding [64]. Here, we fundamentally change the passive binary-amplitude baffle in optics into the active binary-amplitude exciter in acoustics that transforms itself into the feeding. Furthermore, we demonstrate the versatility of our design method, such as the realization of the focal-needle pattern, the multiple-foci pattern and the manipulated

super-oscillatory super resolution in acoustic far fields. Consequently, this approach to manipulate focusing properties is unique in acoustics.

4.6 Conclusion

In conclusion, we propose the method to manipulate the acoustic far-field focusing created with the active and configurable planar metasurface piezoelectric transducer. The designed focal patterns and focal resolutions are demonstrated respectively. By means of the acoustic Rayleigh-Sommerfeld diffraction integral in conjunction with the method of binary particle swarm optimization, a large degree of freedom is obtained to manipulate various far-field focusing phenomena via optimized ring configurations. Here, the pattern of a finite-length focal needle of a subwavelength resolution is designed and realized; another example is the creation of the multiple-foci pattern of a sub-diffraction-limit resolution; for the focal-resolution manipulation, the extremely-high resolution, i.e., the acoustic super-oscillatory super resolution, is demonstrated as well using the prototype of the active and configurable planar metasurface piezoelectric transducer. Due to these significant advantages and versatility, the manipulation of acoustic focusing may offer a reformative framework in medical and industrial technology where the strict control of acoustic high-energy areas is demanding (biomedical actuator, focused ultrasound surgery, lithotripsy, nondestructive testing, etc.).

Chapter 5

Realizing acoustic cloaking and near-zero density with acoustic metastructure

This chapter proposes an acoustic metastructure which has the property of near zero density and is developed for acoustic invisibility cloaking. This acoustic metastructure sustains the characteristics of the reported acoustic cloaks derived by transformation acoustics, and is also able to overcome the defect of topologically-optimized acoustic cloaks. Different from the traditional acoustic metamaterials which have complex (inhomogeneous or anisotropic) components of micro or subwavelength scales, our acoustic metastructure for invisibility cloaking is only made of single-piece homogeneous elastic copper in an accessible layout, including one pressure absorber and one pressure projector connected by an isolated energy channel.

The elastic material can be regarded at a certain resonant frequency as an effective density-near-zero (DNZ) structure. Due to the mechanical resonance of the elastic structure, the phase velocity of sound waves in the cloaking setup almost reaches infinite value, and consequently, extraordinary sound transmission (EST) is expected [65, 66]. The cloaking performance by our acoustic metastructure is explained by simplified theoretical spring-mass model and verified by COMSOL numerical simulation in two-dimensional unbounded space as well as in curved waveguides.

The theoretical explanation of the DNZ property of our proposed metastructure is to be elaborated using the spring-mass models at Section 5.2. In short, DNZ is the consequence of systematic resonances, which result in simultaneous vibration of the entire structure. Therefore, it appears that the vibrational status at one end of the structure can reach to the other end without taking time. The seeming infinite speed of sound can be further paraphrased as the DNZ property.

One limitation of our design is the 1D functionality, i.e., the capability to work only for normal incident waves.

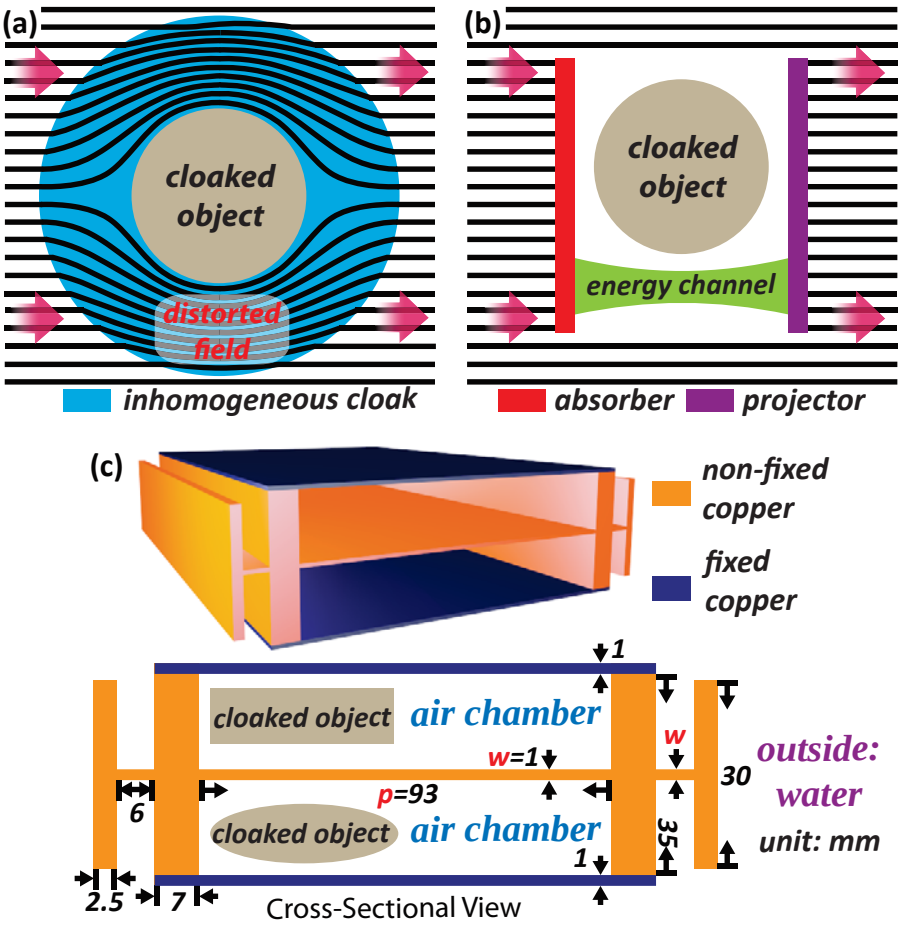

FIGURE 5.1: Comparison of (a) traditional acoustic cloaking based on coordinate transformation and (b) our cloaking by a density-near-zero metastructure for extraordinary sound transmission. (c) Our metastructure consists of one single-piece copper with air chambers inside it, and it is immersed in water. Figure adopted and reproduced with permission from ref. [67].

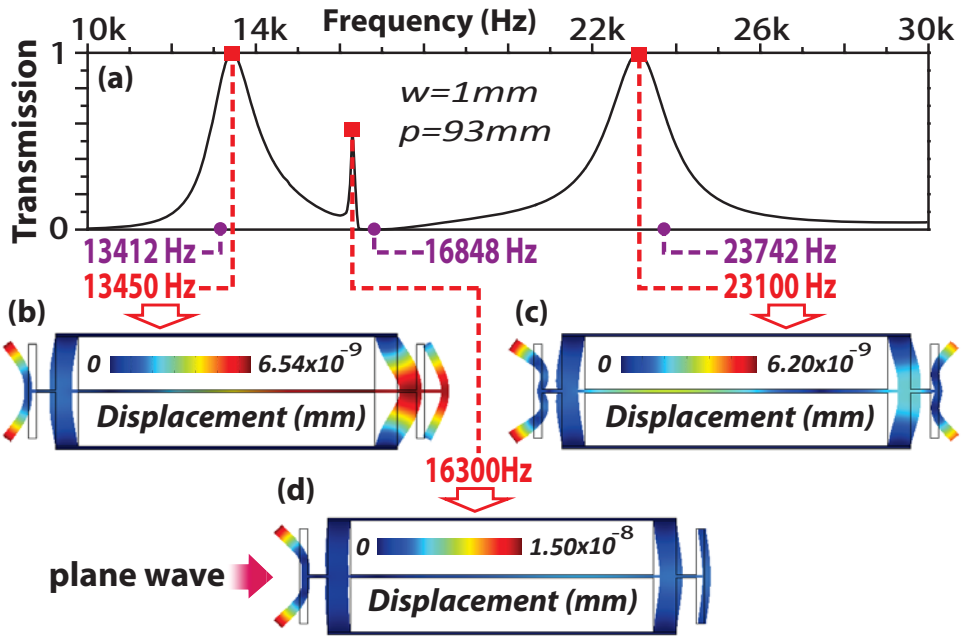

FIGURE 5.2: Simulated sound transmission through the density-near-zero metastructure. The transmission shown in (a) is a function of the frequency of the normally-incident sound waves. The three purple dots indicate the eigen-frequencies of the copper part, and the three red squares indicate the frequencies at the three peaks. The displacement of the structure at input frequencies (three peaks) is shown in (b-d), respectively. Figure adopted and reproduced with permission from ref. [67].

5.1 Metastructure for acoustic cloaking made by copper

To illustrate the concept of our design, we compare it with acoustic cloaking based on coordinate transformation in Figure 5.1(a), which renders an object invisible by distorting its ambient flow. The scheme of the proposed DNZ acoustic-metastructure for cloaking in Figure 5.1(b) can produce EST, to hide arbitrary inserted objects as well as to preserve wavefronts and phases.

Conceptually, the flow at the front of an object is concentrated into the energy channel by an absorber. Then, acoustic energy is coupled out by a projector to the back side where the flow is restored. The entire process resembles the engineering optical camouflage: positioning cameras upon an object wrapped by a retro-reflecting coat; taking pictures and transmitting the signal; projecting the front scene onto the back of the coat [68]. In Figure 5.1(b), acoustic cloaking for 1D invisibility can be achieved without wave distortion along sound paths, and the length of the cloaking device is designed to maintain the phase continuity at both sound inlet and outlet.

The DNZ metastructure for acoustic cloaking shown in Figure 5.1(c) is only implemented by copper (density: $8900kg/m^3$; Youngs modulus: 122GPa; Poissons ratio: 0.35) [42] with two fixed planks (blue parts). p and w are the length and width of the energy channel, respectively. The two hollow enclosed chambers are designed to fill with air (density: $1.21kg/m^3$; speed of sound: $343m/s$), where any objects can be placed inside for the purpose of invisibility. The T-shaped protrusion at each end is used as the locally resonant element to enhance sound transmission [69, 70]. The

entire structure is immersed in water (density: $998kg/m^3$; speed of sound: $1481m/s$), and a monochromatic acoustic plane wave propagates from left to right. The COMSOL software has been used to do simulation.

The acoustic power transmission through the DNZ metastructure for acoustic cloaking immersed in water is numerically simulated. In Figure 5.2(a), there are two frequencies that allow EST (13.45 kHz and 23.1 kHz) with a small peak (16.3 kHz) in between. We also calculate the vibration states at the three frequencies in Figure 5.2(b-d). Figure 5.2(b,c) shows by simulation two opposite resonances of the DNZ metastructure. Inside the metastructure, the internal motion is simply the longitudinal movement of the elastic energy channel, which can be seen at displacement fields. We furthermore individually calculate the eigen-frequencies of the copper parts, shown as the purple dots in Figure 5.2(a). The similarity between the frequencies that correspond to the red squares and that correspond to the purple dots shows that by the systematic resonance the structured metastructure is capable of total power transmission, as the requirement of acoustic cloaking. The slight disagreement between the dots of different colors is because that for the red squares that correspond to Figure 5.2(b,c), the acoustic load from the ambient water has been taken into account, while for the purple dots, we only consider the eigen-frequencies of the copper parts.

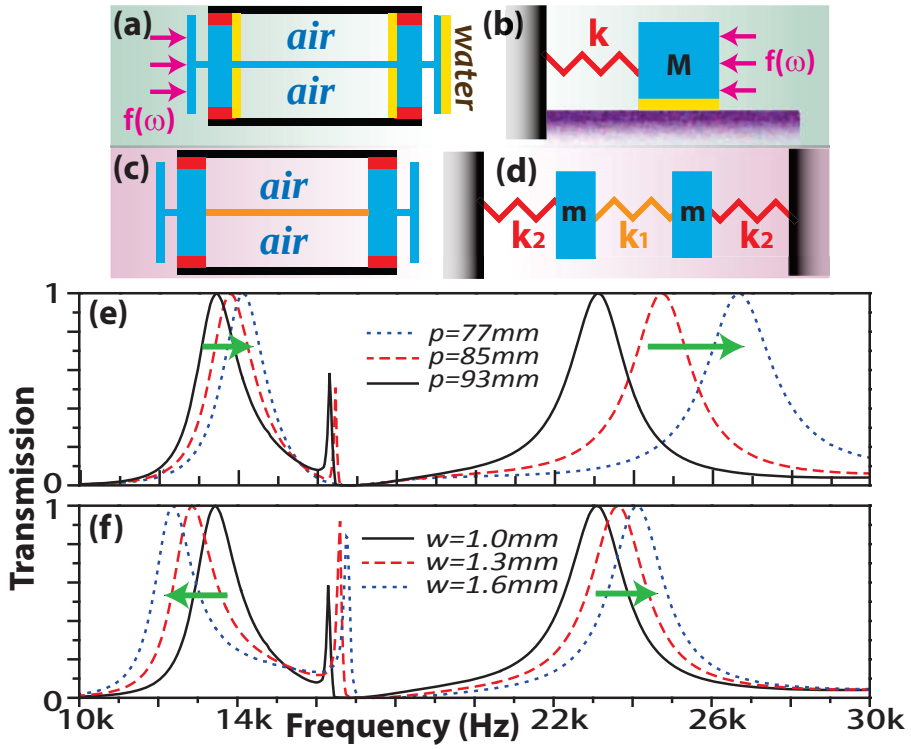

FIGURE 5.3: (a,c) Schematics of the metastructure for acoustic cloaking. Different colors stand for different parts of the metastructure. (b) The spring-mass model. (d) The coupling model. (e,f) The power transmission as a function of the input sound frequency when the shape of the energy channel is changed. Figure adopted and reproduced with permission from ref. [67].

5.2 Spring-mass model and density-near-zero property

Our design focuses on achieving the DNZ property by using the structural resonance, and meanwhile isolating the objects to be hidden from the entire resonance system. A spring-mass model, the mechanical translation of acoustic systems, is illustrated here to expound the resonance and the consequent DNZ property.

The metastructure immersed in water in Figure 5.3(a) can be regarded as the damping spring-mass model in Figure 5.3(b). In Figure 5.3(a), different parts of the metastructure are tinted with different colors to illustrate the counterpart elements in Figure 5.3(b). Specifically, we regard the fixed copper planks (black) as the fixed wall (black), the input sound as the driving force (pink), and the main body of the metastructure as the mass chunk (blue). The joints (red) as well as the elasticity of the metastructure are rationally modeled as the ideal spring (red). The acoustic impedance exerted upon boundaries (yellow) is modeled as frictional damping, because when the metastructure vibrates it will fight against the resistance from the outside water and the inside air. Therefore, the equation for this spring-mass model becomes:

$$Md^2x/dt^2 = -kx - \gamma M dx/dt + F_0 \cos \omega t, \tag{5.1}$$

where k denotes the stiffness of the ideal spring in Figure 5.3(b); γ is the damping coefficient; M is the mass of the chunk; x is the displacement; ω is the driving frequency and $F_0 \cos \omega t$ is the driving force. The

resonant frequency in the case of no damping is $\omega_0 = \sqrt{k/M}$. Then, the solution of Equation (5.1) becomes $x = A\cos(\omega t - \delta)$, where $A = F_0/[M\sqrt{(\omega_0{}^2 - \omega^2)^2 + (\omega\gamma)^2}]$ and $\tan\delta = \omega\gamma/(\omega_0{}^2 - \omega^2)$. The maximum amplitude occurs at $\omega_1 = \sqrt{\omega_0{}^2 - \gamma^2/2}$. If there is no friction $\gamma = 0$, the driving frequency is ω_0 and A goes up infinitely, and the mechanical energy of the vibrating chunk is accumulated because of the driving force. However, if there is a damping effect, e.g. the friction between the ground and the chunk, the accumulated energy at the resonance will be conveyed to dissipation, making the system in its steady state. Under this circumstance, A will remain a finite maximum when $\omega = \omega_1$.

Due to energy conservation, all input power will be consumed by the friction, and the driving energy is transferred wherever the damping (yellow) is. As the comparison in Figure 5.3(a), the force from the input wave not only drives the vibration of the DNZ metastructure, but also needs to overcome the resistances at the solid-liquid interfaces (yellow). Therefore, at systematic resonances, the momentum gain of the acoustic loads, i.e. the inside air and the outside water, consumes all the cumulative input acoustic power. Consequently, at the moment of systematic resonances, the entire system is in its steady state. Note that in order to avoid disturbing the resonances of the metastructure, the objects to be hidden are required to be kept from touching the walls of the chambers.

Moreover, since the acoustic impedance of the outside water is extremely higher than that of the inside air (3561 times), the acoustic load is almost completely attributed by water. Thus, all input power is expected to be transferred to outside water, which leads to EST. The objects inside the

cloaked space are isolated from the systematic resonance of the DNZ metastructure, because the air chambers decouple the systematic resonance from the existence of the inside objects. The decoupling effect is not considered by the traditional design of membrane-induced DNZ metamaterials [66]. However, the proposed metastructure is not able to cloak objects from airborne sound. Because the acoustic forces exerted upon the inside and outside air are comparable, the vibration of the metastructure will result in sound penetration to both inside and outside, which makes the cloaking effect in airborne sound fail.

Instead of the major resonances, there are several other minor resonances due to the rich oscillation modes of solids, which are not observable simply based on simplified 1D spring-mass model. However, the spring-mass model is the classic approach to explain the underlying mechanism of EST and the cause of the acoustic cloaking effect in our design.

Additionally, the spring-mass model implies the DNZ property of the metastructure at its resonance, which is the acoustic equivalent of an electromagnetic epsilon-near-zero metamaterial [71]. We may define the effective mass of the vibration system as $M_{eff}(\omega) = M - k/\omega^2$, which intrinsically includes the acoustic inertance caused by its mass as well as the acoustic compliance caused by its elasticity. The combination of the acoustic compliance and the inertance is the exact analog of the combination of spring compliance and substantial mass in a spring-mass model.

Since the restoring force from the elastic copper of our structure is able to add a negative term to the effective mass, we can rearrange Equation (5.1) considering the harmonic vibration [65]:

$$F_0 \cos \omega t - \gamma M dx/dt \ = M_{eff}(\omega) d^2x/dt^2 \ , \tag{5.2}$$

which turns into the form of Newton's second law: driving force − resistance = mass$\times d^2x/dt^2$. At systematic resonance, $M_{eff}(\omega) = M - k/\omega^2$ becomes zero, so that power transmission of input sound is expected to be extremely enhanced [65]. The causality from the DNZ property of our structure to the resultant EST was elaborated in Ref. [65] where a similar membrane-mass model was proposed. (The detailed derivation of the transmission coefficient was given in the Ref. [65] using the lumped element approach.) Actually, the DNZ effect is an innate property of a dynamic structure with a certain eigen-vibration excited. For our proposed structure, the DNZ metastructure at resonance is explained by the aid of the damping spring-mass model in Figure 5.2(a,b).

However, it is noteworthy that although the dynamic density of the individual metastructure is near zero, the acoustic impedance of the entire acoustic cloaking setup is not near zero at all. When the system vibrates, there will be additional radiation impedance exerted at both ends of the metastructure. When the systematic resonances occur, EST surely implies the impedance match between the proposed structure and the surrounding. The impedance match in such case is dominantly attributed by the radiation impedance, apart from the minor contribution from the DNZ structure itself. Thus, if taken into account the radiation impedance, the overall acoustic impedance is no more near zero.

5.3 Coupling model and geometrical dependence

After discussing the mechanism of the DNZ metastructure for acoustic cloaking, we further examine the geometrical dependence of the power transmission spectrum, by employing the coupling model in Figure 5.3(c,d).

As discussed in Figure 5.3(a,b), the fixed copper planks in Figure 5.3(c) (black) can be modeled as the two hard walls (black) in Figure 5.3(d). To investigate the dependence between the structural geometry and the resonance, the main bodies in Figure 5.3(c) are modeled separately. In this way, the two copper bodies (blue) are modeled as the two chunks (blue) with mass m. The four joints (red) indicating elasticity are interpreted as the two ideal springs (red) with stiffness k_2, connecting the chunks to the walls. Additionally, owing to the narrowness of the energy channel (orange), we model it as the spring with stiffness k_1 and mass m_s (orange), which couples the two chunks. By the coupling model, we discover the dependence between the structural geometry of the DNZ metastructure and the working frequencies of EST.

The equations for the coupling model shown in Figure 5.3(c,d) are:

$$\begin{cases} md^2x_1/dt^2 = -k_2x_1 + k_1(x_2 - x_1) - \gamma m dx_1/dt \\ md^2x_2/dt^2 = -k_1(x_2 - x_1) - k_2x_2 - \gamma m dx_2/dt \end{cases}, \tag{5.3}$$

where x_1 and x_2 are the displacements of the left and the right chunks. The lower and higher resonant frequencies of Equation (5.3) are $\omega_L =$

$\sqrt{k_2/(m+m_s)\ -\gamma^2/4}$ and $\omega_H = \sqrt{(2k_1+k_2)/(m+m_s)\ -\gamma^2/4}$, respectively. If the energy-channel length $p = 93mm$ in Figure 5.1(c) becomes longer, m_s will become larger but k_1 will get smaller, similarly to the serial connection of springs. Therefore, both ω_L and ω_H will become smaller, which implies that all resonant frequencies of the DNZ metastructure will be shifted lower when p becomes longer. Vice versa, if the energy-channel length is shortened the resonant frequencies will be shifted higher. The shift observed from the curves in Figure 5.3(e) validates the theoretical spring-model analysis.

If the channel width $w = 1.0mm$ becomes thicker, m_s as well as k_1 will become larger, similarly to the shunt connection of springs. Therefore, ω_L will become even lower. As for ω_H, the double increments of k_1 at the numerator $(2k_1 + k_2)$ is empirically larger than the increment of m_s at the denominator, leading to the rise of ω_H. Thus, we can predict that if w gets thicker, the low resonant frequencies of the DNZ metastructure will be shifted even lower, whereas the high resonant frequencies will be even higher. The broadening of the power transmission spectrum in Figure 5.3(f) verifies our analysis.

We investigate the geometrical dependence in terms of the sound-tunneling channel inside the metastructure, which is the key component of our structure. However, the two terminal chunks of the metastructure cannot be straightforwardly characterized by spring-mass model. The solid eigenvibration of the chunks are 2D, which is hard to be interpreted by 1D model. The precise analysis of the solid chunks needs direct numerical simulation.

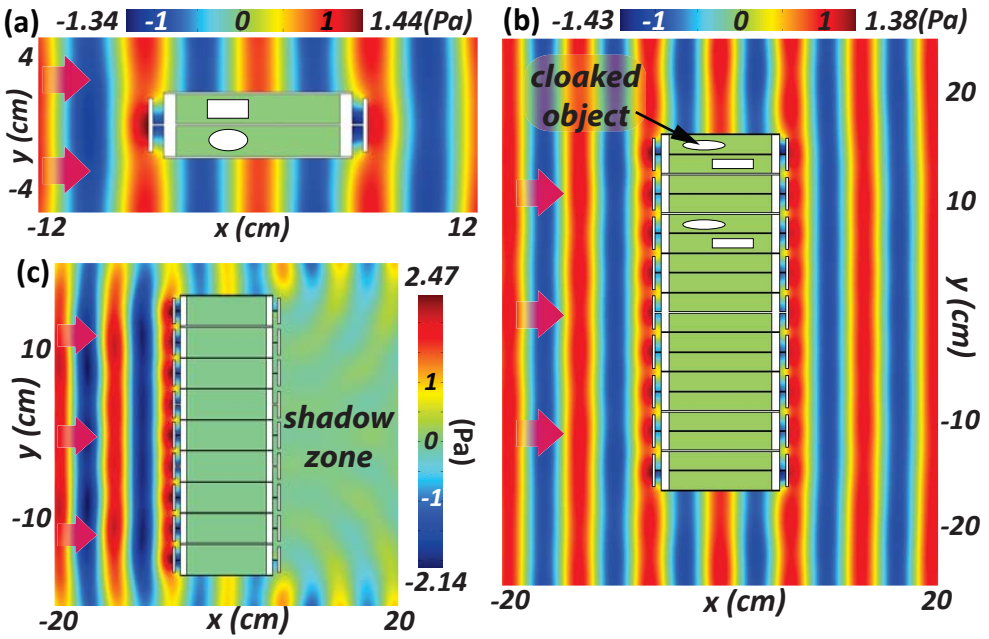

FIGURE 5.4: Applying the metastructure for acoustic cloaking in unbounded space filled with water. (a) Two objects are hidden inside the metastructure. There is no sound inside air chambers, and the field outside the metastructure is almost unperturbed. (b) The density-near-zero array is immersed in water, and the wavefront and the phase are restored at its back. Figure adopted and reproduced with permission from ref. [67].

5.4 Deploying cloaked area in free space and in waveguides

We numerically examine the acoustic pressure field distribution in the domain where the proposed DNZ metastructure is immersed in water, while the monochromatic acoustic waves are normally incident from left with unit magnitude and frequency 23.1 kHz. As expected, inside the air chambers in Figure 5.4(a), there is no sound penetration, which means the inserted objects are isolated and decoupled to the systematic resonance and the outside field. It is remarkable that the power transmission nearly reaches 100%, which implies EST through the DNZ metastructure with no back-scattering.

Also, we notice in Figure 5.4(a) that the phase at the inner side of the T-shaped ends is not continuous because of the perturbation from the local resonances inside the concave of the T-shaped ends. However, the phase at the outer side of the T-shaped ends is almost the same as the adjacent ambient phase. The length of the metastructure is also designed to maintain the phase continuity at the sound outlet, which makes the plane wavefront instead of other curved wavefront propagate out.

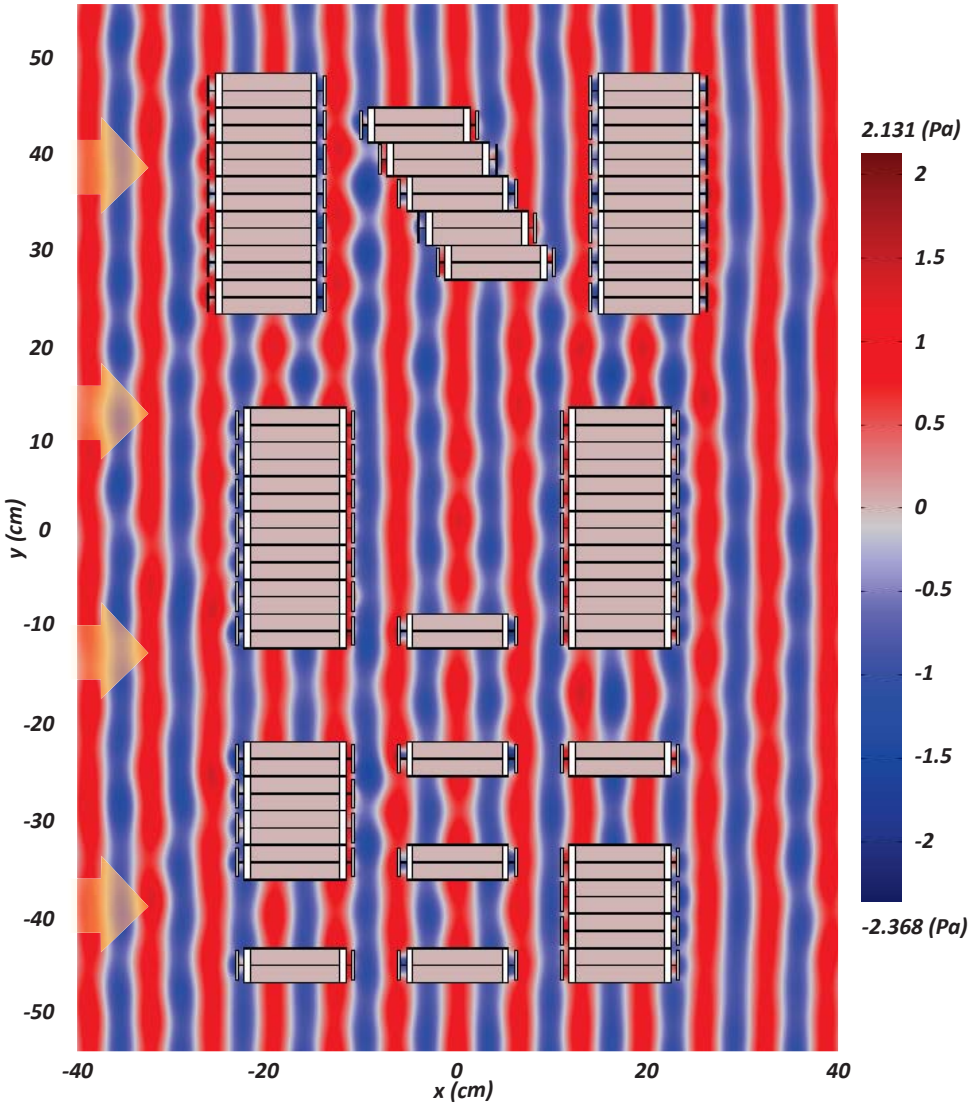

FIGURE 5.5: Multiple metastructures form an "NUS"-shaped cloaked space. Figure adopted and reproduced with permission from ref. [67].

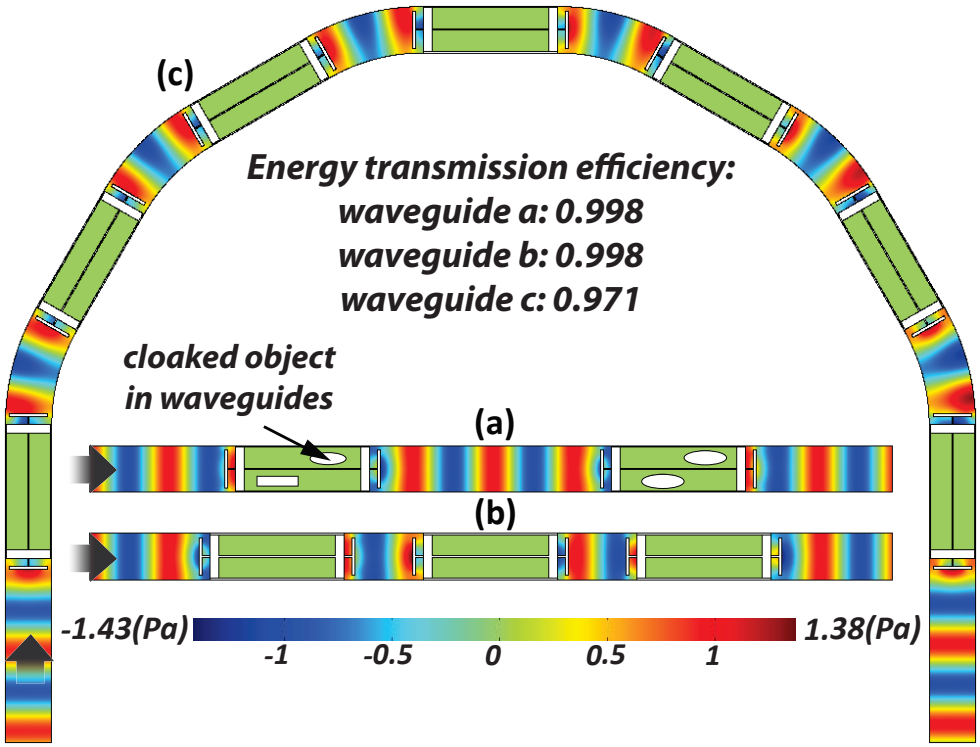

FIGURE 5.6: Applying the metastructure for acoustic cloaking in waveguides. (a) Four objects in a straight waveguide are hidden inside the metastructures. There is no sound inside air chambers, and the outside traveling sound is largely transmitted. (b) The number of metastructures does not affect the resonant frequencies. (c) The high power transmission shows that the metastructures are able to hide inside objects as well as to bend sound in waveguides. Figure adopted and reproduced with permission from ref. [67].

Furthermore, thanks to the rigid boundaries at the two fixed planks in Figure 5.1(c), we can connect as many metastructures sharing the planks as possible, to form an arbitrarily-designed cloaked space. In Figure 5.4(b), the metastructures are aligned side by side to increase the acoustic-cloaking volume. The cloaking effect is demonstrated that the bulky copper array itself and the multiple objects inside the metastructure are imperceptible from outside. Contrarily, if the energy channels are removed, strong back-scattering will occur as shown in Figure 5.4(c). We can also design the overall cloaked space with an arbitrary distribution of the metastructures [see Figure 5.5 where an NUS-shaped cloaked space is formed]. Based on the proposed detachable DNZ metastructures, we accomplish arbitrary acoustic cloaking in 2D space only by a single kind of uniform isotropic material.

Besides the scenario in a 2D space, sound manipulation in waveguides showed significant applications as well, such as the acoustic circulator based on non-reciprocity [72]. Here, the proposed DNZ metastructure is also functional in cloaking objects in waveguides. As shown in Figure 5.6(a) where acoustic waves propagate through the hard-wall waveguide filled with water, the objects inside the air chambers are imperceptible. Note that one characteristic of DNZ property is that energy tunneling occurs independently of the number of DNZ segments, because each DNZ segment is able to resonate at the same frequency without influencing each other [66]. Even if we add more metastructures inside the waveguide, the resonant frequency will not be shifted, as shown in Figure 5.6(b). The energy transmission is almost 100% in both Figure 5.6(a,b), which indicates EST happens through DNZ metastructures. In Figure 5.6(c), we further demonstrate the acoustic

cloaking effect along a curved waveguide, which is used to bend sound path and to maintain the cloaking effect simultaneously as designed.

5.5 Conclusion and discussion

We design an acoustic metastructure for invisibility cloaking that has the density-near-zero property, and is able to eliminate the perceptibility of inside objects from underwater sound. Note that the density-near-zero metastructure for acoustic cloaking is built only by a uniform material, while its cloaking effect is independent of the objects inside it. It much simplifies the traditional realization of acoustic cloaking by complex acoustic metamaterials.

The design is inspired by the combination of acoustic inertance and acoustic compliance of the structure at systematic resonances. A plane wavefront is maintained without distortion, and the reflection is dramatically suppressed due to extraordinary sound transmission. Moreover, such density-near-zero metastructures are detachable, and therefore robust in being assembled to change or expand the overall cloaked space with no limit in volume and distribution. The flexibility can be universally applied in unbounded space as well as in waveguides. We believe that the proposed density-near-zero metastructure may open a distinct and concise way to acoustic cloaking by using natural bulky materials.

There is an alternative way of constructing acoustic cloaking devices without using coordinate transformation, which is called the topological-optimization method [40]. A topology-optimized cloak [73] can hide objects inside it from impinging sounds, which is similar to the function of our device. However,

the shortcoming of a topology-optimized cloak is that the shape and distribution of the cloak components are highly sensitive to the positions, quantities, and the shapes of the inside objects to be hidden. For our proposed approach, the metastructure of a DNZ cloak is irrelevant to the inside objects, though it requires two media of large impedance mismatch.

Chapter 6

Future work

Up to now, we have proposed different designs of acoustic metasurface (one-dimensional varying and two-dimensional varying metasurfaces, and active metasurface) and acoustic metastructure, in order to manipulate sound properties as much as we want (sound wavefront, vibrational orientation, acoustic focusing, and density-near-zero property). We also have demonstrated many novel acoustic applications on the basis of our designs, such as acoustic illusion and ipsilateral focusing, conversion from propagating to surface waves, generation of an acoustic focal needle and acoustic far-field multiple foci, super-oscillatory super resolution, and acoustic invisibility cloaking.

In the thesis we demonstrated the theoretical work as well as the simulation results. We are also in the process of experimentally realizing these proposed devices and measuring their performances. One difficulty of engineering implementation is the required high precision. Starting from the metasurface structure that generates the focused acoustic beams, we are using 3D printers to fabricate the device, and the experiment is ongoing with

the collaboration of the Institute of Acoustics in Nanjing, China. The experiment setup includes the signal function generator Agilent 33250A, the amplifier Electronics Innovation, and a movable hydrophone ONDA HNC-1000 controlled by a LABVIEW program for scanning acoustic pressure and phase.

This chapter addresses two possible future plans based on the current research about acoustic metasurface and metastructure. Section 6.1 introduces the possible manipulation of acoustic band gap (Bragg gap and non-Bragg gap) by acoustic periodic metastructure; Section 6.2 extends the manipulation of sound properties to the manipulation of general wave properties in incompressible fluids.

6.1 Manipulation of band gap for sound transmission

Our proposed metastructures and metasurfaces have the property of periodicity. The working frequency, i.e., band gap, is also an important parameter to adjust for improving the performances of our devices. The generation of pass-bands and stop-bands in periodic structures is commonly attribute to the Bragg resonances, which can be interpreted as the cumulative reflection from each unit of the structure. For a periodic acoustic waveguide, the evanescence of the waves is caused by the typical Bragg resonances.

When the periodicity is comparable to the radial scale of a waveguide, the

non-Bragg nature resonances, involving high-order transverse mode interactions, can also play a role in forbidding the wave propagation. Non-Bragg resonances, caused by the interference between the guided modes of different transverse standing-wave profiles in the periodic waveguide, are theoretically predicted in 2003 in a planar electromagnetic waveguide with corrugated walls [74]. For the future work, we may design and implement acoustic periodic metastructures in realizing non-Bragg acoustic band gaps, and investigate the efficient design of the band gap. In detail, the non-Bragg band gap, as a result of the interference between two transverse guided wave modes, could be investigated in an axis-symmetrical and periodic metastructure. The manipulation of acoustic band gap by metastructures may benefit the design of spectrum structures (the location, the width and the depth of band gaps) in the "band gap engineering".

6.2 Manipulation of acoustic properties in stratified fluids

All the previous work are done in the environment of a uniform fluid. One step forward is to carry out the manipulation of acoustic properties in stratified fluids. The typical wave that is able to exist in stratified incompressible fluids is called internal waves. In a global scale, internal waves are commonly generated by tidal flow over seafloor topography, which plays an important role in dissipation and mixing in the interior of oceans [75, 76]. Also, these waves contribute significantly to the global oceanic energy budget [77, 78]. The main contributor to the internal waves is the M_2 tide, a lunar semi-diurnal tide of frequency $\omega = 1.4052 \times 10^{-4}$ rad/s [79]. One

direct numerical simulation of internal wave radiation for tidal flow over synthetic random topography is shown in Figure 6.1. The details of the simulation are elaborated in Appendix D.

If acoustic metasurfaces are placed in deep water, internal waves will distort acoustic signals, resulting in the inefficiency of device's functions. The first step from manipulation of acoustic properties in uniform fluids to manipulation in stratified fluids needs the thorough study of internal waves. We are considering to conduct the laboratory study of steering acoustic propagation in the presence of internal waves. The experiment setup could be: a tank filled with a stratified fluid containing a wave-maker that generates internal waves, and an acoustic track crossing the internal wave beams. The measurements can be designed to provide a benchmark for a better understanding of the influence of internal waves on 3D sound propagation. The future work lies in implementing metasurfaces and metastructures in manipulating acoustic properties in stratified fluids.

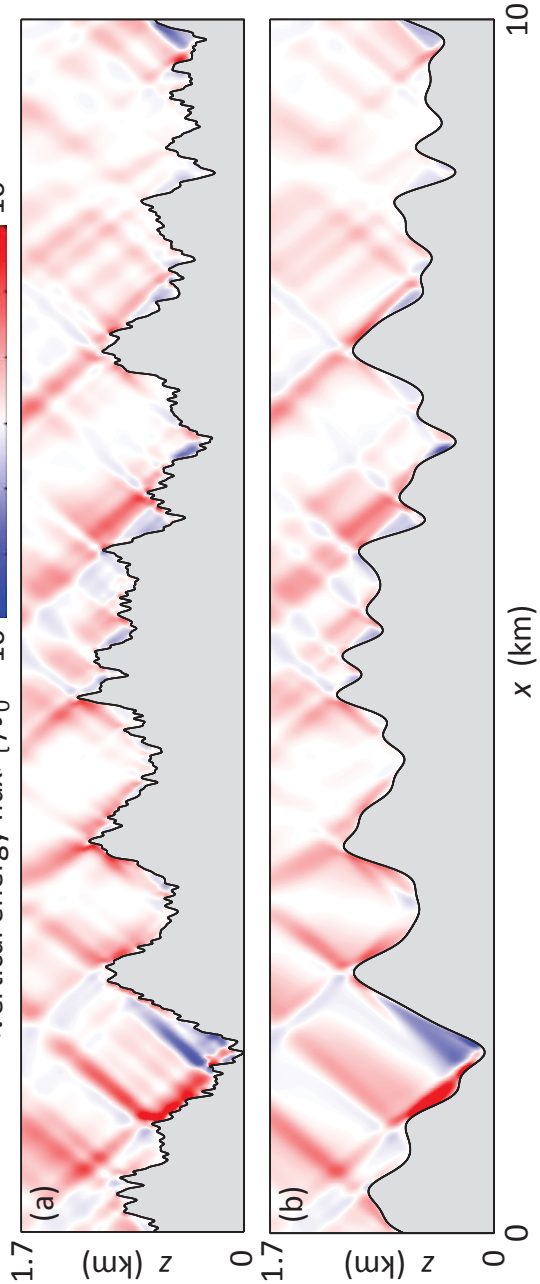

FIGURE 6.1: Direct numerical simulation of internal wave radiation for tidal flow over synthetic random topography, resolved in (a) to 39 m [256 cycles/(10 km)] and in (b) to 312 m [32 cycles/(10 km)]. The vertical component of the normalized internal wave energy flux averaged over a tidal period is shown in red for upward flux and blue for downward (the normalization factor J_0 is the total internal wave power generated in (a) divided by the 10 km length of the topography).

Appendix A

Detailed derivation of impedance-governed generalized Snell's law of reflection (IGSL) in acoustics

We mathematically derive the connection between the interface specific acoustic impedance (SAI) and the manipulation of wavefronts, which gives birth to the proposed impedance-governed generalized Snell's law of reflection (IGSL) as the design rule of SAI. In addition, we mathematically predict the double reflections and the situation when the ordinary reflection can be switched off.

We assume the time-harmonic factor in this appendix is $e^{-i\omega t}$, where ω is the circular frequency, and the coordinate system is that in Figure. A.1(a). The incident acoustic pressure can be expressed as:

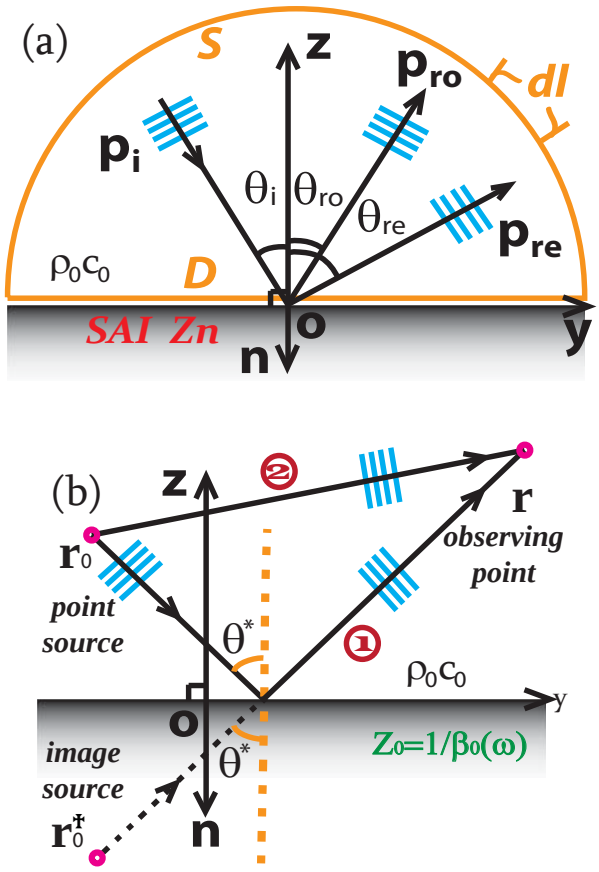

FIGURE A.1: (a) Illustration for some notations. The orange line indicates the contour of the Green's integral. S is the semicircular contour; D is the flat one along the surface. p_i, p_{ro} and p_{re} denote the incidence, the ordinary reflection, and the extraordinary reflection, respectively. $\mathbf{n}$ is the unit vector opposite to z direction. Z_n is set for the flat interface ($z = 0$). (b) Schematic diagram for the effective paths of acoustic radiation. The introduced θ^* can be interpreted as the effective incident angle. $\mathbf{r}$, $\mathbf{r}_0$, and $\mathbf{r}_0^\dagger$ are the location vectors for the point source, the image source and the observer, respectively.

$$p_i(y, z, \omega) = p_{i0}(\omega) \exp[ik_0(y \sin\theta_i - z \cos\theta_i)], \tag{A.1}$$

where $k_0 = \omega/c_0$ is the wave number in free space, θ_i the incident angle and $p_{i0}(\omega)$ the amplitude. $Z_n(y, \omega) = p(y, 0, \omega)/[\mathbf{n} \cdot \mathbf{v}(y, 0, \omega)]$ as the specific acoustic impedance (SAI) [42] of a locally reacting boundary is laid at the interface, where $\mathbf{n}$ is the unit vector opposite to z direction and $\mathbf{v}$ is the acoustic velocity. The boundary condition of this problem can be paraphrased as [80]:

$$\frac{\partial}{\partial z} p(y, 0, \omega) + ik_0 \beta(y, \omega) p(y, 0, \omega) = 0, \tag{A.2}$$

where $\beta(y, \omega) = \rho_0 c_0 / Z_n(y, \omega)$ (ρ_0 and c_0 being the given density and sound speed respectively in the upper space) is the normalized acoustical admittance of the locally reacting surface.

We expand β to be $\beta(y, \omega) = \tilde{\beta}(y, \omega) + \beta_0(\omega)$, where β_0 is a real constant. The ordinary reflection is expressed as:

$$p_{ro}(y, z, \omega) = p_{i0}(\omega) R(\theta_i, \beta_0) \exp[ik_0(y \sin\theta_{ro} + z \cos\theta_{ro})], \tag{A.3}$$

where R is the reflection coefficient and θ_{ro} the angle of p_{ro}. Because p_{ro} observes the usual Snell's law, $\theta_{ro} = \theta_i$. In order to find the expression of R, we introduce the constant SAI:

$$Z_0(\omega) = \frac{\rho_0 c_0}{\beta_0(\omega)} = \frac{p_i(y, 0, \omega) + p_{ro}(y, 0, \omega)}{\mathbf{n} \cdot \mathbf{v}_i(y, 0, \omega) + \mathbf{n} \cdot \mathbf{v}_{ro}(y, 0, \omega)}, \tag{A.4}$$

where $\mathbf{n}$ is the normal vector indicated in Figure. A.1(a), $\mathbf{v}_i$ and $\mathbf{v}_{ro}$ the acoustic velocities of p_i and p_{ro}. Substituting Equation. (A.1) and Equation. (A.3) into Equation. (A.4) and applying Euler equation $\rho_0 \frac{\partial}{\partial t}\mathbf{v} = -\nabla p$, we obtain:

$$R(\theta_i, \beta_0) = \frac{\cos\theta_i - \beta_0(\omega)}{\cos\theta_i + \beta_0(\omega)}. \tag{A.5}$$

In Figure. A.1(a), the total acoustic field can be written in the integral form:

$$\begin{aligned} p(y,z,\omega) = \oint_{S+D} dl[G(y,z,\omega;y_0,z_0)\frac{\partial}{\partial n_0}p(y_0,z_0,\omega) \\ - p(y_0,z_0,\omega)\frac{\partial}{\partial n_0}G(y,z,\omega;y_0,z_0)], \end{aligned} \tag{A.6}$$

where $dl(y_0, z_0)$ is the infinitesimal segment along the integral contour, $\mathbf{n}_0 = \mathbf{n}(y_0, z_0)$ and $G(y, z, \omega; y_0, z_0)$ is the Green's function corresponding to the following partial differential problem:

$$\begin{aligned} &\nabla^2 G + {k_0}^2 G = -\delta(y-y_0)\delta(z-z_0), z > 0 \\ &[\tfrac{\partial}{\partial z_0}G + ik_0\beta_0(\omega)G]\Big|_{z_0=0} = 0 \end{aligned}. \tag{A.7}$$

When the radius of the semicircular contour S approaches ∞, we can regard the contour integral along S is mainly contributed by p_i and p_{ro}. Therefore Equation. (A.6) changes to be:

$$\begin{aligned} p(y,z,\omega) = p_i(y,z,\omega) + p_{ro}(y,z,\omega) \\ - \int_{-\infty}^{\infty} dy_0[G\frac{\partial}{\partial z_0}p(y_0,z_0,\omega) - p(y_0,z_0,\omega)\frac{\partial}{\partial z_0}G]. \end{aligned} \tag{A.8}$$

We can simplify Equation. (A.8) by substituting Equation. (A.7) and Equation. (A.2) into it. By defining the last part in Equation. (A.9) as the extraordinary reflection $p_{re}(y, z, \omega)$, which is the unique extra component beyond p_{ro}, we obtain

$$p_{re}(y, z, \omega) = ik_0 \int_{-\infty}^{\infty} \tilde{\beta}(y_0, \omega) p(y_0, 0, \omega) G(y, z, \omega; y_0, 0) dy_0. \tag{A.9}$$

The explicit solution of $G(y, z, \omega; y_0, z_0)$ in Equation. (A.7) is

$$\begin{aligned} G = & \frac{i}{4} H_0^{(1)}(k_0 |\mathbf{r} - \mathbf{r}_0|) \\ & + \frac{i}{4\pi} \int_{-\infty}^{\infty} \frac{1}{k_z} \frac{k_z - \omega\beta_0/c_0}{k_z + \omega\beta_0/c_0} \exp[ik_z(z + z_0) + ik_y(y - y_0)] dk_y, \end{aligned} \tag{A.10}$$

where $\mathbf{r} = (y, z)$, $\mathbf{r}_0 = (y, z)$, and ${k_0}^2 = {k_y}^2 + {k_z}^2$. When $\mathbf{r}$ is away from the surface D, $k_z \approx k_0 \cos\theta^*$ holds, where θ^* is introduced as a constant. Via this approximation and another definition $\mathbf{r}_0^\dagger = (y_0, -z_0)$, it turns out that [54]

$$\cos\theta^* \approx \frac{z - (-z_0)}{\left|\mathbf{r} - \mathbf{r}_0^\dagger\right|} \approx constant. \tag{A.11}$$

Through Equation. (A.11), it can be obtained that

$$\frac{k_z - \omega\beta_0/c_0}{k_z + \omega\beta_0/c_0} \approx \frac{\cos\theta^* - \beta_0(\omega)}{\cos\theta^* + \beta_0(\omega)} \approx constant \approx R(\theta^*, \beta_0). \tag{A.12}$$

Applying Equation. (A.12) into Equation. (A.10) and using the formula of the cylindrical wave expansion in terms of plane waves, we approach a neat form of the Green's function:

$$G(y,z,\omega;y_0,z_0) \approx \frac{i}{4}H_0^{(1)}(k_0\left|\mathbf{r}-\mathbf{r}_0\right|)+R(\theta^*,\beta_0)\frac{i}{4}H_0^{(1)}(k_0\left|\mathbf{r}-\mathbf{r}_0^{\dagger}\right|), \quad \text{(A.13)}$$

where $H_0^{(1)}(\cdot)$ the Hankel function of the first kind. [81]

From the physical insight into Equation. (A.13), the first part of G is the direct contribution of the point source to the observer through path 2 in Figure. A.1(b). The second part is the product of the Green's function excited by the image source and the reflection coefficient R, denoting p_{ro}. According to our interpretation, Figure. A.1(b) illustrates path 1 and path 2, visualized as p_{ro} and p_{re} respectively[54]. Due to the expression of R, we figure out that θ^* is the effective incident angle regarding to Figure. A.1(b). Furthermore, it is reasonable to say that the major contribution of the integral in Equation. (A.10) is attributed to the vicinity of θ^*, in which way R can be regarded as a constant and put outside the integral.

By far-field approximation, we are able to get these expansions:

$$\begin{aligned}
\mathbf{r}\cdot\mathbf{r}_0 &= r(y_0\sin\theta + z_0\cos\theta)\\
\mathbf{r}\cdot\mathbf{r}_0^{\dagger} &= r(y_0\sin\theta - z_0\cos\theta)\ ,\\
H_0^{(1)}(x)\Big|_{x\to\infty} &\approx \sqrt{\tfrac{2}{\pi x}}e^{i(x-\frac{\pi}{4})}
\end{aligned} \quad \text{(A.14)}$$

where r is the length of $\mathbf{r}$; $\sin\theta = y/r$; $\cos\theta = z/r$. Substituting Equation. (A.14) and Equation. (A.5) into Equation. (A.13), we obtain:

$$G(y,z,\omega;y_0,0) \approx i\sqrt{\frac{1}{2\pi k_0 r}}e^{i(k_0 r-\frac{\pi}{4})}e^{-ik_0 y_0\sin\theta}\frac{\cos\theta^*}{\cos\theta^*+\beta_0(\omega)}. \quad \text{(A.15)}$$

After substituting Equation. (A.15) into Equation. (A.9), the extraordinary reflection becomes:

$$p_{re} \approx -\sqrt{\frac{k_0}{2\pi r}} e^{i(k_0 r - \frac{\pi}{4})} \frac{\cos\theta^*}{\cos\theta^* + \beta_0(\omega)} \int_{-\infty}^{\infty} \tilde{\beta}(y_0, \omega) p(y_0, 0, \omega) e^{-ik_0 y_0 \sin\theta_{re}} dy_0. \tag{A.16}$$

Further, after applying Born approximation to Equation. (A.16) and expanding it by Equation. (A.1) and Equation. (A.3), p_{re} becomes:

$$\begin{aligned} p_{re} \approx -\sqrt{\frac{2k_0}{\pi r}} \times \frac{p_{i0}(\omega) \exp[i(k_0 r - \frac{\pi}{4})] \cos\theta^* \cos\theta_i}{[\cos\theta^* + \beta_0(\omega)][\cos\theta_i + \beta_0(\omega)]} \\ \times \int_{-\infty}^{\infty} \tilde{\beta}(y_0, \omega) e^{ik_0 y_0 (\sin\theta_i - \sin\theta_{re})} dy_0. \end{aligned} \tag{A.17}$$

Now we consider our proposed SAI:

$$Z_n(y, \omega) = A\left[1 - i\tan\frac{\psi(y)}{2}\right]; \beta_0(\omega) = \frac{\rho_0 c_0}{2A}. \tag{A.18}$$

After substituting Equation. (A.18) into Equation. (A.3) and Equation. (A.17), we obtain the ordinary reflection and the extra reflection: extraordinary reflection:

$$p_{ro} \propto \frac{2A\cos\theta_i - \rho_0 c_0}{2A\cos\theta_i + \rho_0 c_0} \exp[ik_0(y\sin\theta_{ro} + z\cos\theta_{ro})], \tag{A.19}$$

$$p_{re} \propto \int_{-\infty}^{\infty} e^{i\psi(y)} e^{ik_0 y(\sin\theta_i - \sin\theta_{re})} dy. \tag{A.20}$$

Here note that in our case we are able to create *double reflections* by means of SAI inhomogeneity.

Equation. (A.20) is a Dirac Delta if we consider $\psi(y)$ to be a linear term as the first order approximation. Or else, we know that the integral in Equation. (A.20) will reach the maximum by imposing the stationary phase approximation, i.e.,

$$\sin\theta_{re} - \sin\theta_i = \frac{1}{k_0}\frac{d\psi(y)}{dy}. \tag{A.21}$$

Although Equation. (A.21) corresponds to the form of the generalized Snell's law of reflection (GSL) [1], the variables in the two situations are different. Starting from Equation. (A.18) and ending up with Equation. (A.21), we provide the insight between our designed SAI and the direction of p_{re}, without considering the phase in terms of wave propagation. We name Equation. (A.21) as IGSL in acoustics, as the design principle of the SAI Equation. (A.18).

According to Equation. (A.19), if $A = (\rho_0 c_0)/(2\cos\theta_i)$, we can switch off p_{ro}. Therefore Equation. (A.18) becomes

$$Z_n(y,\omega) = \frac{\rho_0 c_0}{2\cos\theta_i}\left[1 - i\tan\frac{\psi(y)}{2}\right]. \tag{A.22}$$

Appendix B

Distinction of IGSL in acoustics

The same appearance of the impedance-governed generalized Snell's law of reflection (IGSL) and the generalized Snell's law of reflection (GSL) may cause the false impression that our IGSL is the same as GSL. Actually their mechanisms are totally distinct.

In terms of phase inhomogeneity, the anomalous reflection p_{ra} actually corresponds to the situation when the ordinary reflection p_{ro} is steered toward a "wrong" direction governed by GSL [1], illustrated in Figure. B.1(a). There is only one single direction of reflection all the while. On the contrary in terms of SAI inhomogeneity, it is found that IGSL cannot alter p_{ro} by an SAI interface, but can "turn off" p_{ro} so as to provide insight into the engineering of special wavefronts by SAI interface, illustrated in Figure. B.1(b). Moreover, the extraordinary reflection p_{re} governed by IGSL is an additionally unique component in acoustics, which can be "geared"

along arbitrary directions, simultaneously with vanishing p_{ro}. Therefore, our proposed IGSL opens up rich effects and unprecedented applications in the community of acoustics. Additionally, GSL can even be considered as one subset of IGSL, when p_{ro} is turned off. In order to stress the irrelevance between IGSL and GSL again, we list the differences:

1. GSL is initiated in electromagnetism with electric properties; IGSL is initiated in acoustics with mechanical properties.

2. GSL is derived from Fermat Principle, i.e., the conservation of the wave number along an interface; IGSL is derived from Green's function. The fundamental physics is distinguished.

3. The variable of GSL is phase inhomogeneity; the variable of IGSL is impedance inhomogeneity. The methods are independent.

4. GSL will only generate single reflection; IGSL not only can generate single reflection, but also can generate double reflections.

5. GSL acts upon p_{ro}; IGSL acts upon p_{re}.

6. In GSL, the anomalous reflection corresponds to the situation where p_{ro} is tweaked toward a different direction governed by GSL; in acoustics, IGSL cannot alter p_{ro} by SAI interfaces, but is capable of "turning on" or "turning off" p_{ro}.

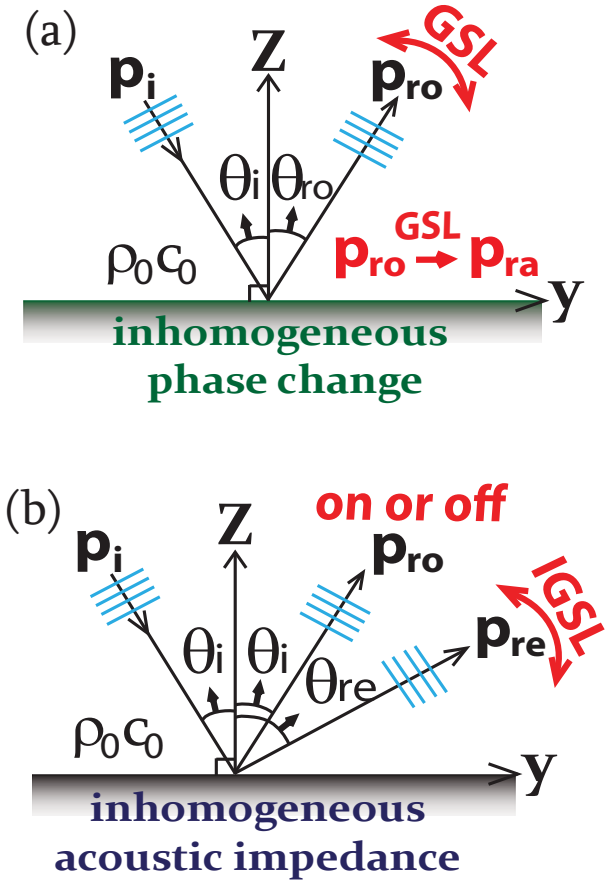

FIGURE B.1: (a) For a flat interface with an inhomogeneous phase change, the angle of p_{ro}, i.e., θ_{ro}, is tweaked in a fashion of GSL. The manipulated "ordinary reflection" is called to be the anomalous reflection p_{ra} in terms of GSL. [1] (b) For a flat interface with an inhomogeneous SAI, $\theta_{ro} = \theta_i$ without influence, while p_{re} occurs simultaneously and θ_{re} is controlled by IGSL, implying double reflections. If SAI is properly controlled, p_{ro} can be switched off.

Appendix C

Parameters of metasurface piezoelectric transducer

C.1 Parameters of Lead Zirconate Titanate PZT-5H

The density of PZT-5H is 7500 kg/m^3.

Table C.1: Symmetric elasticity matrix (Pa)

1.27×10^{11}	8.02×10^{10}	8.47×10^{10}	0	0	0
0	1.27×10^{11}	8.47×10^{10}	0	0	0
0	0	1.17×10^{11}	0	0	0
0	0	0	2.30×10^{10}	0	0
0	0	0	0	2.30×10^{10}	0
0	0	0	0	0	2.35×10^{10}

Table C.2: Relative permittivity ε_{Sr}

1704.4	0	0
0	1704.4	0
0	0	1433.6

Table C.3: Coupling matrix e (C/m^2)

0	0	0	0	17.0345	0
0	0	0	17.0345	0	0
-6.6228	-6.6228	23.2403	0	0	0

C.2 Optimized configuration of ring pattern

Table C.4: Configuration of 30 rings to generate a focal needle (mm)

r1	2.95	r7	36.68	r13	71.28	r19	102.62	r25	137.42
rr1	7.07	rr7	40.79	rr13	75.39	rr19	106.74	rr25	141.54
r2	8.19	r8	43.37	r14	76.35	r20	109.67	r26	143.69
rr2	12.31	rr8	47.49	rr14	80.47	rr20	113.78	rr26	147.81
r3	13.27	r9	49.20	r15	81.39	r21	114.91	r27	150.20
rr3	17.39	rr9	53.32	rr15	85.51	rr21	119.02	rr27	154.32
r4	19.32	r10	56.02	r16	86.77	r22	120.05	r28	156.36
rr4	23.44	rr10	60.13	rr16	90.89	rr22	124.17	rr28	160.48
r5	24.66	r11	60.79	r17	92.76	r23	126.30	r29	161.12
rr5	28.78	rr11	64.90	rr17	96.88	rr23	130.41	rr29	165.23
r6	30.33	r12	66.25	r18	97.84	r24	131.53	r30	167.04
rr6	34.45	rr12	70.36	rr18	101.95	rr24	135.65	rr30	171.16

Table C.5: Configuration of 28 rings to generate multiple foci (mm)

r1	6.86	r8	49.05	r15	107.70	r22	171.84
rr1	10.98	rr8	53.17	rr15	111.82	rr22	175.96
r2	13.03	r9	55.22	r16	116.96	r23	183.50
rr2	17.15	rr9	59.34	rr16	121.08	rr23	187.62
r3	17.49	r10	63.80	r17	123.82	r24	194.14
rr3	25.73	rr10	67.92	rr17	127.94	rr24	198.26
r4	27.44	r11	72.37	r18	131.71	r25	201.34
rr4	31.56	rr11	76.49	rr18	135.83	rr25	205.46
r5	32.58	r12	79.92	r19	143.03	r26	216.09
rr5	36.70	rr12	84.04	rr19	147.15	rr26	220.21
r6	37.04	r13	86.78	r20	156.06	r27	230.49
rr6	41.16	rr13	90.90	rr20	160.18	rr27	238.73
r7	42.53	r14	95.69	r21	164.64	r28	244.90
rr7	46.65	rr14	99.81	rr21	168.76	rr28	249.02

Table C.6: Configuration of 19 rings to generate super-oscillatory super resolution (mm)

r1	5.33	r6	46.56	r11	91.79	r16	136.87
rr1	9.61	rr6	50.84	rr11	96.08	rr16	141.15
r2	11.77	r7	55.50	r12	99.74	r17	145.58
rr2	16.05	rr7	59.79	rr12	104.03	rr17	149.87
r3	19.97	r8	64.13	r13	111.33	r18	151.41
rr3	24.26	rr8	68.42	rr13	115.61	rr18	155.69
r4	29.33	r9	72.18	r14	118.42	r19	159.96
rr4	33.62	rr9	76.47	rr14	122.71	rr19	167.56
r5	39.35	r10	81.53	r15	128.72		
rr5	43.64	rr10	85.82	rr15	133.01		

Appendix D

Details of the simulation for internal waves

We conduct direct numerical simulations for tidal flow over synthetic random topography. The computational domain of width 10 km has periodic boundary conditions on the sides and a no-slip boundary condition on the random bottom topography. Wave reflection from the top boundary of the domain is avoided by adding a Rayleigh damping force that gradually increases upward. The damping force starts from a height of 5 km and goes up to the domain top of 15.5 km height; the approximately 3×10^6 control volumes have unstructured grids.

The simulations use the CDP 2.4 code, which implements a fractional-step time-marching scheme [82]. This code with disabled sub-grid modeling and an addition of buoyancy forces has been used and validated in previous studies of IW generation by tidal flow in stratified fluids [83–85]. Tidal flow is produced by adding a horizontal force, $F(t) = \rho_0 U_0 \omega cos(\omega t)$, to the

momentum equation. We use $U_0 = 0.14$ cm/s, resulting in a tidal excursion close to $U_0/\omega = 10$ m. The small excursion relative to the autocorrelation widths of the topographies is chosen to avoid overturning and turbulence, since the interest here is in the radiation. The viscosity, $\nu = 0.01m^2/s$, is four orders larger than that of water to reduce the simulation cost (sparser grids are needed for higher ν); however, the large viscosity has a negligible effect on tidal conversion in the regime of laminar flow [84]. The salt diffusivity κ is $2 \times 10^{-5}m^2/s$, which gives negligible diffusion for the large Schmidt number, $\nu/\kappa = 500$. Each simulation has 2000 time steps per period and extends for 20 tidal periods to ensure a steady state. The convergence is tested by doubling the spatial and temporal resolution; this changes the computed IW power by less than 3%.

The radiated IW power is calculated from the horizontal integral of the vertical energy flux averaged over a tidal period, $\Phi_z(x,z) \equiv \langle p'\mathbf{v}' \rangle_t$ at $z = z_{top}$, where z_{top} is the maximum topographic height, p' is the wave pressure, and $\mathbf{v}'$ is the wave velocity, given by $\mathbf{v}'(x,z,t) = \mathbf{v}(x,z,t) - \mathbf{v}_{baro}(z,t)$, where $\mathbf{v}(x,z,t)$ is the fluid velocity and $\mathbf{v}_{baro}(z,t)$ is the barotropic velocity, which in our simulations is approximated by $U_0 sin(\omega t)$ because our domain height is much taller than the topographic height (thus the flow acceleration over the topography is negligible). An example of the time-averaged energy flux field $\Phi_z(x,z)$ from our simulations is shown in Figure 6.1(a).

Bibliography

[1] N. Yu, P. Genevet, M. A. Kats, F. Aieta, J.-P. Tetienne, F. Capasso, and Z. Gaburro, "Light propagation with phase discontinuities: generalized laws of reflection and refraction," *Science*, vol. 334, no. 6054, pp. 333–337, 2011.

[2] B. Sundar, A. C. Hamilton, and J. Courtial, "Fermat's principle and the formal equivalence of local light-ray rotation and refraction at the interface between homogeneous media with a complex refractive index ratio," *Optics Letters*, vol. 34, no. 3, pp. 374–376, 2009.

[3] S. Larouche and D. R. Smith, "Reconciliation of generalized refraction with diffraction theory," *Optics Letters*, vol. 37, no. 12, pp. 2391–2393, 2012.

[4] J. Zhao and Z.-Y. Tao, "Fine-tuning of nonbragg bandgaps in axisymmetric ducts via arbitrary periodic walls," *Journal of Sound and Vibration*, vol. 332, no. 25, pp. 6541–6551, 2013.

[5] X. Ni, N. K. Emani, A. V. Kildishev, A. Boltasseva, and V. M. Shalaev, "Broadband light bending with plasmonic nanoantennas," *Science*, vol. 335, no. 6067, pp. 427–427, 2012.

[6] M. Kang, T. Feng, H.-T. Wang, and J. Li, "Wave front engineering from an array of thin aperture antennas," *Optics Express*, vol. 20, no. 14, pp. 15882–15890, 2012.

[7] F. Aieta, P. Genevet, M. A. Kats, N. Yu, R. Blanchard, Z. Gaburro, and F. Capasso, "Aberration-free ultrathin flat lenses and axicons at telecom wavelengths based on plasmonic metasurfaces," *Nano Letters*, vol. 12, no. 9, pp. 4932–4936, 2012.

[8] L. Huang, X. Chen, H. Muhlenbernd, G. Li, B. Bai, Q. Tan, G. Jin, T. Zentgraf, and S. Zhang, "Dispersionless phase discontinuities for controlling light propagation," *Nano Letters*, vol. 12, no. 11, pp. 5750–5755, 2012.

[9] P. Genevet, N. Yu, F. Aieta, J. Lin, M. A. Kats, R. Blanchard, M. O. Scully, Z. Gaburro, and F. Capasso, "Ultra-thin plasmonic optical vortex plate based on phase discontinuities," *Applied Physics Letters*, vol. 100, no. 1, p. 013101, 2012.

[10] N. Engheta, "Antenna-guided light," *Science*, vol. 334, no. 6054, pp. 317–318, 2011.

[11] M. Born and E. Wolf, *Principles of optics: electromagnetic theory of propagation, interference and diffraction of light*. Cambridge university press, 1999.

[12] E. Hecht, *Optik*. McGraw-Hill, 1987.

[13] J. Achenbach, *Wave propagation in elastic solids*. Elsevier, 2012.

[14] G. Clement, P. White, and K. Hynynen, "Enhanced ultrasound transmission through the human skull using shear mode conversion," *The*

Journal of the Acoustical Society of America, vol. 115, no. 3, pp. 1356–1364, 2004.

[15] J. Li and C. Chan, "Double-negative acoustic metamaterial," *Physical Review E*, vol. 70, no. 5, p. 055602, 2004.

[16] Y. Lai, Y. Wu, P. Sheng, and Z.-Q. Zhang, "Hybrid elastic solids," *Nature Materials*, vol. 10, no. 8, pp. 620–624, 2011.

[17] F. Falcone, T. Lopetegi, M. Laso, J. Baena, J. Bonache, M. Beruete, R. Marqués, F. Martin, and M. Sorolla, "Babinet principle applied to the design of metasurfaces and metamaterials," *Physical Review Letters*, vol. 93, no. 19, p. 197401, 2004.

[18] S. Sun, Q. He, S. Xiao, Q. Xu, X. Li, and L. Zhou, "Gradient-index meta-surfaces as a bridge linking propagating waves and surface waves," *Nature Materials*, vol. 11, no. 5, pp. 426–431, 2012.

[19] X. Chen, L. Huang, H. Mühlenbernd, G. Li, B. Bai, Q. Tan, G. Jin, C.-W. Qiu, S. Zhang, and T. Zentgraf, "Dual-polarity plasmonic metalens for visible light," *Nature Communications*, vol. 3, p. 1198, 2012.

[20] J. Hao, Y. Yuan, L. Ran, T. Jiang, J. A. Kong, C. Chan, and L. Zhou, "Manipulating electromagnetic wave polarizations by anisotropic metamaterials," *Physical Review Letters*, vol. 99, no. 6, p. 063908, 2007.

[21] S.-J. Song, H. J. Shin, and Y. H. Jang, "Development of an ultra sonic phased array system for nondestructive tests of nuclear power plant components," *Nuclear Engineering and Design*, vol. 214, no. 1, pp. 151–161, 2002.

[22] S. Chatillon, G. Cattiaux, M. Serre, and O. Roy, "Ultrasonic non-destructive testing of pieces of complex geometry with a flexible phased array transducer," *Ultrasonics*, vol. 38, no. 1, pp. 131–134, 2000.

[23] S. W. Shin, A. R. Qureshi, J.-Y. Lee, and C. B. Yun, "Piezoelectric sensor based nondestructive active monitoring of strength gain in concrete," *Smart Materials and Structures*, vol. 17, no. 5, p. 055002, 2008.

[24] B. Jaffe, *Piezoelectric ceramics*, vol. 3. Elsevier, 2012.

[25] W. Liu and X. Ren, "Large piezoelectric effect in pb-free ceramics," *Physical Review Letters*, vol. 103, no. 25, p. 257602, 2009.

[26] E.-K. Kim, C. S. Park, W. Y. Chung, K. K. Oh, D. I. Kim, J. T. Lee, and H. S. Yoo, "New sonographic criteria for recommending fine-needle aspiration biopsy of nonpalpable solid nodules of the thyroid," *American Journal of Roentgenology*, vol. 178, no. 3, pp. 687–691, 2002.

[27] J. E. Kennedy, "High-intensity focused ultrasound in the treatment of solid tumours," *Nature Reviews Cancer*, vol. 5, no. 4, pp. 321–327, 2005.

[28] E. A. Stewart, W. M. Gedroyc, C. M. Tempany, B. J. Quade, Y. Inbar, T. Ehrenstein, A. Shushan, J. T. Hindley, R. D. Goldin, M. David, *et al.*, "Focused ultrasound treatment of uterine fibroid tumors: safety and feasibility of a noninvasive thermoablative technique," *American Journal of Obstetrics and Gynecology*, vol. 189, no. 1, pp. 48–54, 2003.

[29] M. A. Averkiou and R. O. Cleveland, "Modeling of an electrohydraulic lithotripter with the kzk equation," *The Journal of the Acoustical Society of America*, vol. 106, no. 1, pp. 102–112, 1999.

[30] B. W. Drinkwater and P. D. Wilcox, "Ultrasonic arrays for non-destructive evaluation: A review," *Ndt & E International*, vol. 39, no. 7, pp. 525–541, 2006.

[31] J. Wang, W. Chen, and Q. Zhan, "Engineering of high purity ultra-long optical needle field through reversing the electric dipole array radiation," *Optics Express*, vol. 18, no. 21, pp. 21965–21972, 2010.

[32] M. Friese, T. Nieminen, N. Heckenberg, and H. Rubinsztein-Dunlop, "Optical alignment and spinning of laser-trapped microscopic particles," *Nature*, vol. 394, no. 6691, pp. 348–350, 1998.

[33] N. H. Gokhale, J. L. Cipolla, and A. N. Norris, "Special transformations for pentamode acoustic cloaking," *The Journal of the Acoustical Society of America*, vol. 132, no. 4, pp. 2932–2941, 2012.

[34] A. Norris and A. Shuvalov, "Elastic cloaking theory," *Wave Motion*, vol. 48, no. 6, pp. 525–538, 2011.

[35] D. Schurig, J. Mock, B. Justice, S. A. Cummer, J. B. Pendry, A. Starr, and D. Smith, "Metamaterial electromagnetic cloak at microwave frequencies," *Science*, vol. 314, no. 5801, pp. 977–980, 2006.

[36] A. N. Norris, "Acoustic cloaking theory," in *Proceedings of the Royal Society of London A: Mathematical, Physical and Engineering Sciences*, vol. 464, pp. 2411–2434, The Royal Society, 2008.

[37] S. Zhang, C. Xia, and N. Fang, "Broadband acoustic cloak for ultrasound waves," *Physical Review Letters*, vol. 106, no. 2, p. 024301, 2011.

[38] B.-I. Popa, L. Zigoneanu, and S. A. Cummer, "Experimental acoustic ground cloak in air," *Physical Review Letters*, vol. 106, no. 25, p. 253901, 2011.

[39] V. M. García-Chocano, L. Sanchis, A. Díaz-Rubio, J. Martínez-Pastor, F. Cervera, R. Llopis-Pontiveros, and J. Sánchez-Dehesa, "Acoustic cloak for airborne sound by inverse design," *Applied Physics Letters*, vol. 99, no. 7, p. 074102, 2011.

[40] L. Sanchis, V. García-Chocano, R. Llopis-Pontiveros, A. Climente, J. Martínez-Pastor, F. Cervera, and J. Sánchez-Dehesa, "Three-dimensional axisymmetric cloak based on the cancellation of acoustic scattering from a sphere," *Physical Review Letters*, vol. 110, no. 12, p. 124301, 2013.

[41] J. Zhao, B. Li, Z. Chen, and C.-W. Qiu, "Manipulating acoustic wavefront by inhomogeneous impedance and steerable extraordinary reflection," *Scientific Reports*, vol. 3, 2013.

[42] D. T. Blackstock, *Fundamentals of physical acoustics*. John Wiley & Sons, 2000.

[43] Y. Li, B. Liang, X. Tao, X.-f. Zhu, X.-y. Zou, and J.-c. Cheng, "Acoustic focusing by coiling up space," *Applied Physics Letters*, vol. 101, no. 23, p. 233508, 2012.

[44] J. Renger, M. Kadic, G. Dupont, S. S. Aćimović, S. Guenneau, R. Quidant, and S. Enoch, "Hidden progress: broadband plasmonic invisibility," *Optics Express*, vol. 18, no. 15, pp. 15757–15768, 2010.

[45] C. Zhang and T. J. Cui, "Negative reflections of electromagnetic waves in a strong chiral medium," *Applied Physics Letters*, vol. 91, no. 19, p. 194101, 2007.

[46] D. Fattal, J. Li, Z. Peng, M. Fiorentino, and R. G. Beausoleil, "Flat dielectric grating reflectors with focusing abilities," *Nature Photonics*, vol. 4, no. 7, pp. 466–470, 2010.

[47] J. Zhu, Y. Chen, X. Zhu, F. J. Garcia-Vidal, X. Yin, W. Zhang, and X. Zhang, "Acoustic rainbow trapping," *Scientific Reports*, vol. 3, 2013.

[48] D.-D. Dai and X.-F. Zhu, "An effective gauge potential for nonreciprocal acoustics," *Europhysics Letters*, vol. 102, no. 1, p. 14001, 2013.

[49] Y. Li, B. Liang, Z.-m. Gu, X.-y. Zou, and J.-c. Cheng, "Reflected wavefront manipulation based on ultrathin planar acoustic metasurfaces," *Scientific Reports*, vol. 3, 2013.

[50] Y. Li, X. Jiang, R.-q. Li, B. Liang, X.-y. Zou, L.-l. Yin, and J.-c. Cheng, "Experimental realization of full control of reflected waves with subwavelength acoustic metasurfaces," *Physical Review Applied*, vol. 2, no. 6, p. 064002, 2014.

[51] J. Zhao, B. Li, Z. N. Chen, and C.-W. Qiu, "Redirection of sound waves using acoustic metasurface," *Applied Physics Letters*, vol. 103, no. 15, p. 151604, 2013.

[52] F. Mechel, "On sound absorption of finite-size absorbers in relation to their radiation impedance," *Journal of Sound and Vibration*, vol. 135, no. 2, pp. 225–262, 1989.

[53] F. P. Mechel, *Formulas of acoustics*, vol. 2. Springer Science & Business Media, 2002.

[54] G. Taraldsen, "The complex image method," *Wave Motion*, vol. 43, no. 1, pp. 91–97, 2005.

[55] J. J. Sakurai and J. Napolitano, *Modern quantum mechanics*. Addison-Wesley, 2011.

[56] H. Wang, L. Shi, B. Lukyanchuk, C. Sheppard, and C. T. Chong, "Creation of a needle of longitudinally polarized light in vacuum using binary optics," *Nature Photonics*, vol. 2, no. 8, pp. 501–505, 2008.

[57] R. Castellano and L. Feinstein, "Ion-beam deposition of thin films of ferroelectric lead zirconate titanate (pzt)," *Journal of Applied Physics*, vol. 50, no. 6, pp. 4406–4411, 1979.

[58] J. Zhao, H. Ye, K. Huang, Z. N. Chen, B. Li, and C.-W. Qiu, "Manipulation of acoustic focusing with an active and configurable planar metasurface transducer," *Scientific Reports*, vol. 4, 2014.

[59] B. A. Auld, *Acoustic fields and waves in solids*, vol. 2. RE Krieger, 1990.

[60] E. T. Rogers, J. Lindberg, T. Roy, S. Savo, J. E. Chad, M. R. Dennis, and N. I. Zheludev, "A super-oscillatory lens optical microscope for subwavelength imaging," *Nature Materials*, vol. 11, no. 5, pp. 432–435, 2012.

[61] H. Ye, C.-W. Qiu, K. Huang, J. Teng, B. Lukyanchuk, and S. P. Yeo, "Creation of a longitudinally polarized subwavelength hotspot with an

ultra-thin planar lens: vectorial rayleigh–sommerfeld method," *Laser Physics Letters*, vol. 10, no. 6, p. 065004, 2013.

[62] N. Jin and Y. Rahmat-Samii, "Advances in particle swarm optimization for antenna designs: Real-number, binary, single-objective and multiobjective implementations," *IEEE Transactions on Antennas and Propagation*, vol. 55, no. 3, pp. 556–567, 2007.

[63] K. Huang, H. Ye, J. Teng, S. P. Yeo, B. Luk'yanchuk, and C.-W. Qiu, "Optimization-free superoscillatory lens using phase and amplitude masks," *Laser & Photonics Reviews*, vol. 8, no. 1, pp. 152–157, 2014.

[64] E. T. Rogers, S. Savo, J. Lindberg, T. Roy, M. R. Dennis, and N. I. Zheludev, "Super-oscillatory optical needle," *Applied Physics Letters*, vol. 102, no. 3, p. 031108, 2013.

[65] J. J. Park, K. Lee, O. B. Wright, M. K. Jung, and S. H. Lee, "Giant acoustic concentration by extraordinary transmission in zero-mass metamaterials," *Physical Review Letters*, vol. 110, no. 24, p. 244302, 2013.

[66] R. Fleury and A. Alù, "Extraordinary sound transmission through density-near-zero ultranarrow channels," *Physical Review Letters*, vol. 111, no. 5, p. 055501, 2013.

[67] J. Zhao, Z. N. Chen, B. Li, and C.-W. Qiu, "Acoustic cloaking by extraordinary sound transmission," *Journal of Applied Physics*, vol. 117, no. 21, p. 214507, 2015.

[68] S. Tachi, "Telexistence and retro-reflective projection technology," in *Proceedings of the 5th Virtual Reality International Conference (VRIC2003)*, vol. 69, pp. 1–69, 2003.

[69] Z. Liu, X. Zhang, Y. Mao, Y. Zhu, Z. Yang, C. Chan, and P. Sheng, "Locally resonant sonic materials," *Science*, vol. 289, no. 5485, pp. 1734–1736, 2000.

[70] L. Yong, L. Bin, Z. Xin-Ye, and C. Jian-Chun, "Broadband acoustic transmission enhancement through a structured stiff plate with locally resonant elements," *Chinese Physics Letters*, vol. 29, no. 11, p. 114301, 2012.

[71] Z. Yang, J. Mei, M. Yang, N. Chan, and P. Sheng, "Membrane-type acoustic metamaterial with negative dynamic mass," *Physical Review Letters*, vol. 101, no. 20, p. 204301, 2008.

[72] R. Fleury, D. L. Sounas, C. F. Sieck, M. R. Haberman, and A. Alù, "Sound isolation and giant linear nonreciprocity in a compact acoustic circulator," *Science*, vol. 343, no. 6170, pp. 516–519, 2014.

[73] J. Andkjær and O. Sigmund, "Topology optimized cloak for airborne sound," *Journal of Vibration and Acoustics*, vol. 135, no. 4, p. 041011, 2013.

[74] V. Pogrebnyak, "Geometric resonance in a periodic waveguide," *Journal of Applied Physics*, vol. 94, no. 10, pp. 6979–6981, 2003.

[75] W. H. Munk, "Abyssal recipes," *Deep Sea Research and Oceanographic Abstracts*, vol. 13, no. 4, pp. 707–730, 1966.

[76] C. Wunsch and R. Ferrari, "Vertical mixing, energy, and the general circulation of the oceans," *Annual Review of Fluid Mechanics*, vol. 36, pp. 281–314, 2004.

[77] S. R. Jayne and L. C. S. Laurent, "Parameterizing tidal dissipation over rough topography," *Geophysical Research Letters*, vol. 28, no. 5, pp. 811–814, 2001.

[78] C. Garrett and E. Kunze, "Internal tide generation in the deep ocean," *Annual Review of Fluid Mechanics*, vol. 39, pp. 57–87, 2007.

[79] M. R. House, "Orbital forcing timescales: an introduction," *Geological Society, London, Special Publications*, vol. 85, no. 1, pp. 1–18, 1995.

[80] M. A. Nobile and S. I. Hayek, "Acoustic propagation over an impedance plane," *The Journal of the Acoustical Society of America*, vol. 78, no. 4, pp. 1325–1336, 1985.

[81] C. Chien and W. Soroka, "Sound propagation along an impedance plane," *Journal of Sound and Vibration*, vol. 43, no. 1, pp. 9–20, 1975.

[82] F. Ham and G. Iaccarino, *Annual Research Briefs 2004*, pp. 3–14. Stanford, CA: Center for Turbulence Research, 2004.

[83] B. King, H. Zhang, and H. L. Swinney, "Tidal flow over three-dimensional topography in a stratified fluid," *Physics of Fluids*, vol. 21, no. 11, p. 116601, 2009.

[84] A. Dettner, H. L. Swinney, and M. Paoletti, "Internal wave and boundary current generation by tidal flow over topography," *Physics of Fluids*, vol. 25, no. 11, p. 116601, 2013.

[85] L. Zhang and H. L. Swinney, "Virtual seafloor reduces internal wave generation by tidal flow," *Physical Review Letters*, vol. 112, no. 10, p. 104502, 2014.